



Riboflavin integrates cellular energetics and cell cycle to regulate maize seed development

Qiuzhen Tian¹, Gang Wang², Xuexia Ma³, Qingwen Shen¹, Mengli Ding¹, Xueyi Yang¹, Xiaoli Luo¹, Rongrong Li¹, Zhenghui Wang¹, Xiangyang Wang¹, Zhiyuan Fu¹ , Qinghua Yang¹, Jihua Tang^{1,4} and Guifeng Wang^{1,*} 

¹National Key Laboratory of Wheat and Maize Crops Science, CIMMYT-Henan Joint Center for Wheat and Maize Improvement, Collaborative Innovation Center of Henan Grain Crops, College of Agronomy, Henan Agricultural University, Zhengzhou, China

²School of Agriculture and Biology, Shanghai Jiao Tong University, Shanghai, China

³Shanghai Key Laboratory of Bio-Energy Crops, School of Life Sciences, Shanghai University, Shanghai, China

⁴The Shennong Laboratory, Zhengzhou, China

Received 23 January 2022;

accepted 10 April 2022.

*Correspondence (Tel +86 371 56990324, fax +86 371 56990188, email: guifeng.wang@henau.edu.cn)

Summary

Riboflavin is the precursor of essential cofactors for diverse metabolic processes. Unlike animals, plants can *de novo* produce riboflavin through an ancestrally conserved pathway, like bacteria and fungi. However, the mechanism by which riboflavin regulates seed development is poorly understood. Here, we report a novel maize (*Zea mays* L.) opaque mutant *o18*, which displays an increase in lysine accumulation, but impaired endosperm filling and embryo development. *O18* encodes a rate-limiting bifunctional enzyme ZmRIBA1, targeted to plastid where to initiate riboflavin biosynthesis. Loss of function of *O18* specifically disrupts respiratory complexes I and II, but also decreases SDH1 flavinylation, and in turn shifts the mitochondrial tricarboxylic acid (TCA) cycle to glycolysis. The deprivation of cellular energy leads to cell-cycle arrest at G1 and S phases in both mitosis and endoreduplication during endosperm development. The unexpected up-regulation of cell-cycle genes in *o18* correlates with the increase of H3K4me3 levels, revealing a possible H3K4me-mediated epigenetic back-up mechanism for cell-cycle progression under unfavourable circumstances. Overexpression of *O18* increases riboflavin production and confers osmotic tolerance. Altogether, our results substantiate a key role of riboflavin in coordinating cellular energy and cell cycle to modulate maize endosperm development.

Keywords: cell cycle, mitochondrion, opaque, riboflavin, seed development.

Introduction

Beyond the essential roles in diverse biochemical pathways, metabolites such as acetyl-CoA, 2-oxoglutarate, and most B vitamins, also serve as co-substrates for many epigenetic masters, thus integrating nutrition, metabolism and gene expression (Kaelin and McKnight, 2013). Riboflavin (Vitamin B₂) generates cofactors, flavin mononucleotide (FMN) and flavin adenine dinucleotide (FAD), which are implicated in many metabolic processes, including electron transport chain, fatty-acid β -oxidation, tricarboxylic acid (TCA) cycle, redox homeostasis, as well as signalling, through oxidation–reduction reactions (Massey, 2000; Pinto and Zemleni, 2016). Importantly, riboflavin deficiency is able to directly cause many human health disorders (Balasubramaniam *et al.*, 2019; Balasubramaniam and Yaplitto-Lee, 2020; Powers, 2003). Therefore, human needs intake of riboflavin from daily diet, in contrast to *de novo* production in plants, fungi and bacteria.

The biosynthesis pathway of riboflavin is highly conserved, initiating from the same precursors, guanosine triphosphate (GTP) and ribulose 5-phosphate (Bacher *et al.*, 2000). Nevertheless, minor evolutionary changes exist in different lineages, with regard to the order of reaction steps and the fusion of riboflavin biosynthesis proteins (RIB) (Fischer and Bacher, 2011; Gerdes *et al.*, 2012). For example, the Gram-positive bacterium *Bacillus subtilis* and plants use a bifunctional enzyme RIBA, having dual GTP cyclohydrolase II (GCH II) and dihydroxybutanone phosphate

synthase (DHBPS) activities, to catalyse the two precursors, in contrast to two split monofunctional enzymes (ribA and ribB) in *Escherichia coli* and yeast. The fusion protein was proposed to have a kinetic advantage for stoichiometrically consuming the two substrates (Moore, 2004). The documentation of riboflavin synthesis and metabolism is comprehensive; yet, its physiological and biological functions are particularly limited in plants.

Like animals, plants lacking riboflavin also cause severe consequences, such as impaired stress defence and defective seed development (Dai *et al.*, 2019; Hanson *et al.*, 2016; Hasnain *et al.*, 2013). Cereal seed originates from the flowering plants-specific double-fertilization event, thereafter generating a diploid embryo and a triploid endosperm. In contrast to most dicots, cereal endosperm is sustained at maturity to store carbohydrates and proteins that are consumed by human and livestock. Proliferation of the endosperm is complicated and dynamic, largely controlled by three distinct modes during cell-cycle progression (Sabelli and Larkins, 2009). It comprises an early acytokinetic mitosis at 2 days after pollination (DAP), resulting in a syncytium that couples to the subsequent cellularization, a short normal mitosis around 7 DAP, and later endoreduplication causing polyploid nuclei. This scenario provides a potentially promising approach for cereal seed improvement, through optimizing the certain endosperm cell cycle.

Here, we characterized a novel soft and starchy endosperm mutant *opaque18* (*o18*) in maize. In contrast to the lack of some essential amino acids in maize seeds, the opaque mutants usually have enhanced nutritional quality, and are elite germplasms to

develop quality protein maize (QPM) (Gibbon and Larkins, 2005; Zhang et al., 2018). So far, at least eight opaque mutants have been characterized and are broadly implicated in zein genes expression (Feng et al., 2018; Schmidt et al., 1990; Zhang et al., 2015), zein protein body assembly (Wang et al., 2012; Yao et al., 2016), and seed metabolism (Myers et al., 2011; Wang et al., 2011, 2014; Yang et al., 2018), which indeed shed insights into the molecular mechanisms underlying endosperm filling and seed yield and quality in cereals.

However, their roles in endosperm cell proliferation and development remain to be fully addressed. O18 is a bifunctional RIBA, having GCH II and DHBPS enzymatic activities, to initiate riboflavin synthesis. In addition to the elevated lysine content, *o18* displays impaired embryo and endosperm development. We present evidence that O18 regulates cell energy metabolism through the mitochondrial respiratory system, and modulates cell-cycle progression through genetic and epigenetic mechanisms, in maize endosperm. Our data shed light on an essential role of riboflavin in coordination of cellular energy, cell cycle and seed development.

Results

A novel maize opaque mutant *o18* displays decreased yield, but enhanced quality

A novel ethylmethane sulphonate (EMS)-mutagenized seed mutant, named dnj*-N1534 (Sheridan and Neuffer, 1983), was obtained from the Maize Genetics Cooperation Stock Center. After being introgressed into W64A background, the top-pale and less-filled seeds were segregated from a self-pollinated

heterozygous plant with a ratio of ~25% (Figure 1a and Table S1). Intriguingly, the mature mutant seeds showed an opaque and starchy appearance (Figure 1b), thereafter termed as *opaque18* (*o18-1*). Embryos were collapsed and disorganized in *o18-1* relative to the wild type (Figure 1c). In agreement, *o18-1* was not able to germinate under normal growth conditions (Figure 1d), indicating that it is embryonically lethal. The hundred-kernel weight of *o18-1* was around 57% of the wild type (Figure 1e), and the endosperm starch content of *o18-1* was reduced to 80% of the wild type (Figure 1f). In contrast to the steady level of total protein, the amount of zein and nonzein in *o18-1* were oppositely altered relative to those in the wild type (Figures 1g and S1). The reduced zein content in turn resulted in a drastic increase in the essential amino acid lysine in *o18-1*, which was 76.4% more than that in the wild type (Figure 1h). Therefore, *o18-1* is a novel and potentially applicable high-lysine maize germplasm, which is achieved by rebalancing seed yield and quality.

Loss of function of *O18* severely impairs endosperm filling and embryo development

During seed development, *o18-1* mutant was discriminated as early as 10 days after pollination (DAP), featured as the top-pale appearance, which was more prominent at the subsequent stages (Figure S2). At the mid-stage (25 DAP), compared with the wild type, *o18-1* mutant was less filled and displayed in part crumple phenotype.

Next, paraffin section was carried out to investigate the cytological differences of developing seeds between *o18-1* and the wild type. At 10 DAP, *o18-1* resembled the wild type in seed

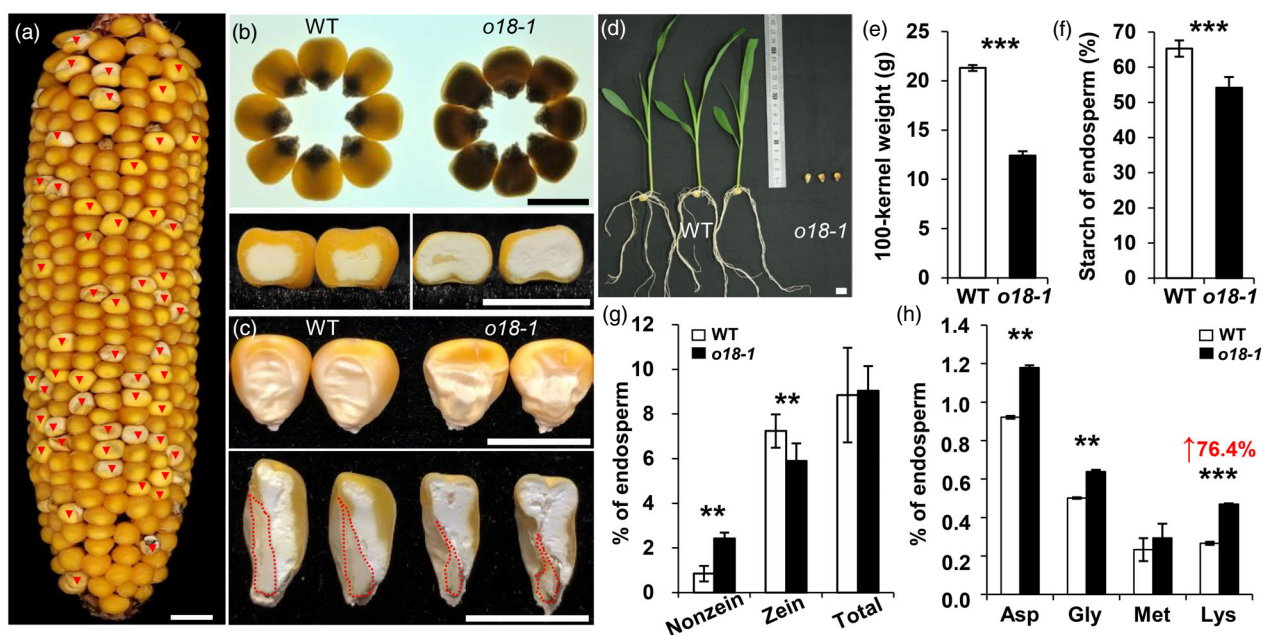


Figure 1 Phenotypic features of the maize *o18-1* mutant. (a) A mature self-pollinated heterozygous ear segregating opaque mutants (red arrows). (b) Mature kernels of the wild type (WT) and *o18-1* mutant observed on a light box (upper) and cross-sections of them (lower). (c) Randomly selected mature WT and *o18-1* mutant kernels and their vertical sections. The red dashed line separates endosperm and embryo. (d) Seedlings of WT and *o18-1* at 12 days after sowing (DAS). (e) Comparison of 100-kernel weight of randomly selected mature WT and *o18-1* kernels in the segregated ears. (f, g) Comparison of starch and protein (nonzein, zein and total protein) contents between WT and *o18-1* mature endosperm. (h) Soluble amino acids with altered contents in WT and *o18-1* mature endosperm. Representative results from at least three biological replicates are shown. Values are means with SE (**, $P < 0.01$; ***, $P < 0.001$, Student's *t*-test). Bars: (a–d) 1 cm.

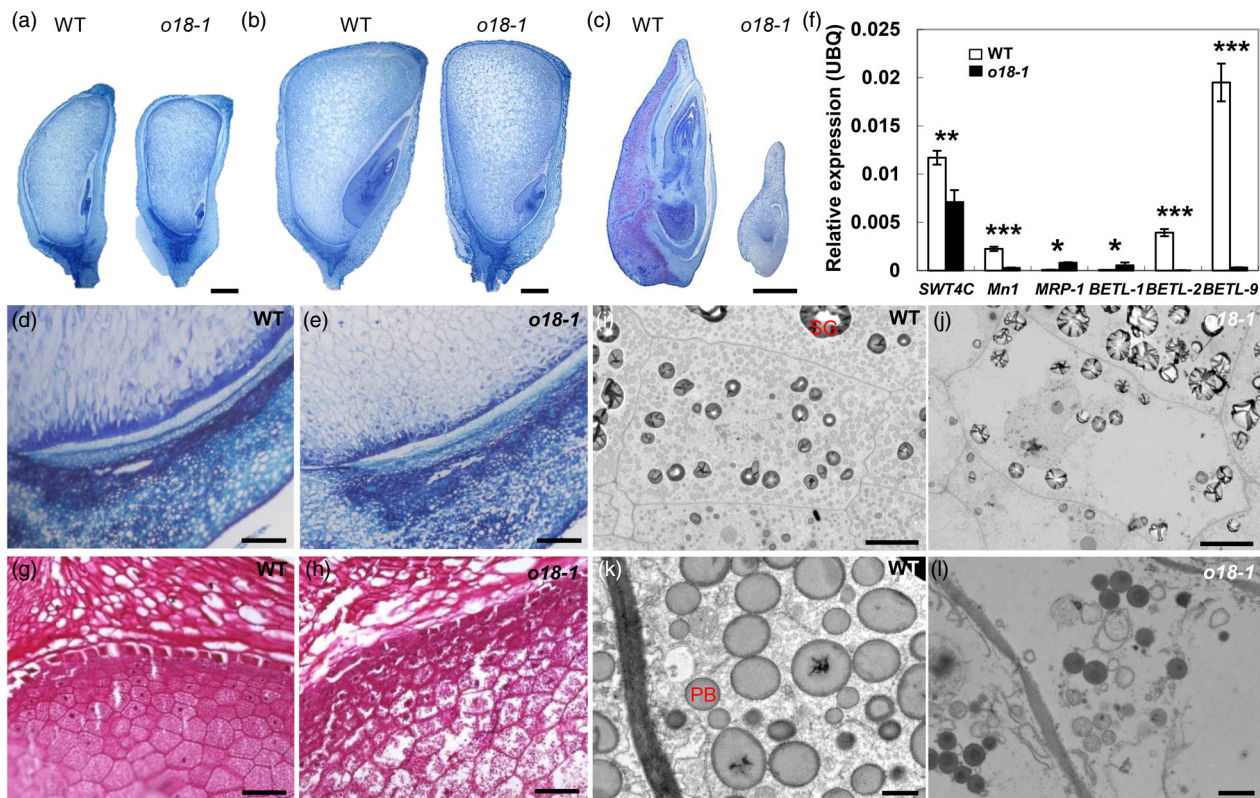


Figure 2 Endosperm filling and embryo development are impaired in *o18-1*. (a) and (b) Paraffin sections of the wild type (WT) and *o18-1* developing kernels from the same segregating ear at 10 DAP (a) and 15 DAP (b). (c) Arrested *o18-1* embryos at 20 DAP. (d, e) Observations of the basal endosperm transfer layer (BETL) of WT (d) and *o18-1* (e), at 10 DAP. (f) Expression levels of BETL-related genes in WT and *o18-1* kernels at 10 DAP. For each RNA sample, three technical replicates were performed. Representative results from three biological replicates are shown. Error bars represent SE. Transcript abundance is indicated relative to the internal control *Ubiquitin (UBQ)*. * $P < 0.05$; ** $P < 0.01$; *** $P < 0.001$, Student's *t*-test. (g, h) Endosperm filling in WT (g) and *o18-1* (h) at 15 DAP. (i, j) Transmission electron microscopy images of endosperm cells in WT (i) and *o18-1* (j) at 20 DAP. SG, starch granule. (k, l) Protein bodies (PBs) in WT (k) and *o18-1* (l). Bars: (a–c) 2 mm; (d, e, g and h) 100 μ m; (i, j) 10 μ m; (k, l) 1 μ m.

size, but its embryo development was drastically retarded (Figure 2a). During filling stage, at 15 DAP, the seed size of *o18-1* became smaller than the wild type (Figure 2b). Notably, the embryo development of *o18-1* stopped at around one or two leaf primordium stage at 20 DAP, in contrast to the fully developed embryo in wild type (Figure 2c). The basal endosperm transfer layer (BETL) of *o18-1* comprised only a single layer of cells with aberrant cell wall ingrowths (Figure 2d,e). In agreement, the expression of BETL marker genes in *o18-1* was significantly down-regulated at 10 DAP (Figure 2f), but was greatly induced at late stages (Figure S3), relative to the wild type. These data suggested a possible negative feedback loop controlling the expression of the BETL regulators. Nevertheless, it was not able to overturn the maternal nutrition allocation defects, as illustrated by the less-filled starch granules in *o18-1* endosperm cells (Figure 2g,h). Transmission electron microscopic investigation further revealed that the mutant endosperm cells were filled with fewer protein bodies (Figure 2i,j). Also, their sizes were drastically reduced, featured as dark staining in *o18-1* (Figure 2k,l). Together, *O18* is required for both embryo and endosperm development.

Positional cloning and validation of *O18*

A map-based cloning approach was used to isolate the *O18* gene by using an F_2 population, with molecular markers listed in Table S2. We initially positioned *o18* in the long arm of

Chromosome 5 and further narrowed down to a physical region of 140 kb (Figure 3a), between markers Indel F05-25 (10 recombinants) and dCAPs236 (1 recombinant). Gene annotation identified 18 putative open reading frames (ORFs) (Table S3), according to the B73 RefGen_v4 genome (Jiao *et al.*, 2017).

Sequencing analysis revealed that a G-to-A transition at exon 4 of *Zm00001d016902* could result in a residue substitution from G-to-E (Figures 3b and S4A). We further confirmed that this mutation is specific to *o18-1*, by screening 120 maize inbred lines with a derived dCAPs marker (Figure S4B). Another EMS-mutagenized mutant (*o18-2*, stock EMS3-05e806-F4) (Lu *et al.*, 2018) was identified to have a C-to-T transition at exon 2, thus generating the residue from a Q to a premature stop codon (Figures 3b and S4C). Ears from self-pollinated heterozygous *o18-2* and reciprocal crosses between $+/o18-1$ and $+/o18-2$ segregated defective seeds at a ratio of ~25% (Figure 3c and Table S4), indicating that they are mutually allelic. Moreover, a CRISPR-Cas9-derived mutant, named as *o18-3*, had a 5-bp deletion in the boundary of exon 2-intron 2 (Figures 3b and S4D), which in turn caused a splicing error. Likewise, self-crossed ears of heterozygous *o18-3* plants segregated defective seeds at a ratio of ~25%, and it was also allelic to *o18-1* by using the reciprocally crossing tests (Figure 3d and Table S4). Taken together, these data confirmed that *Zm00001d016902* is the casual gene for *o18*.

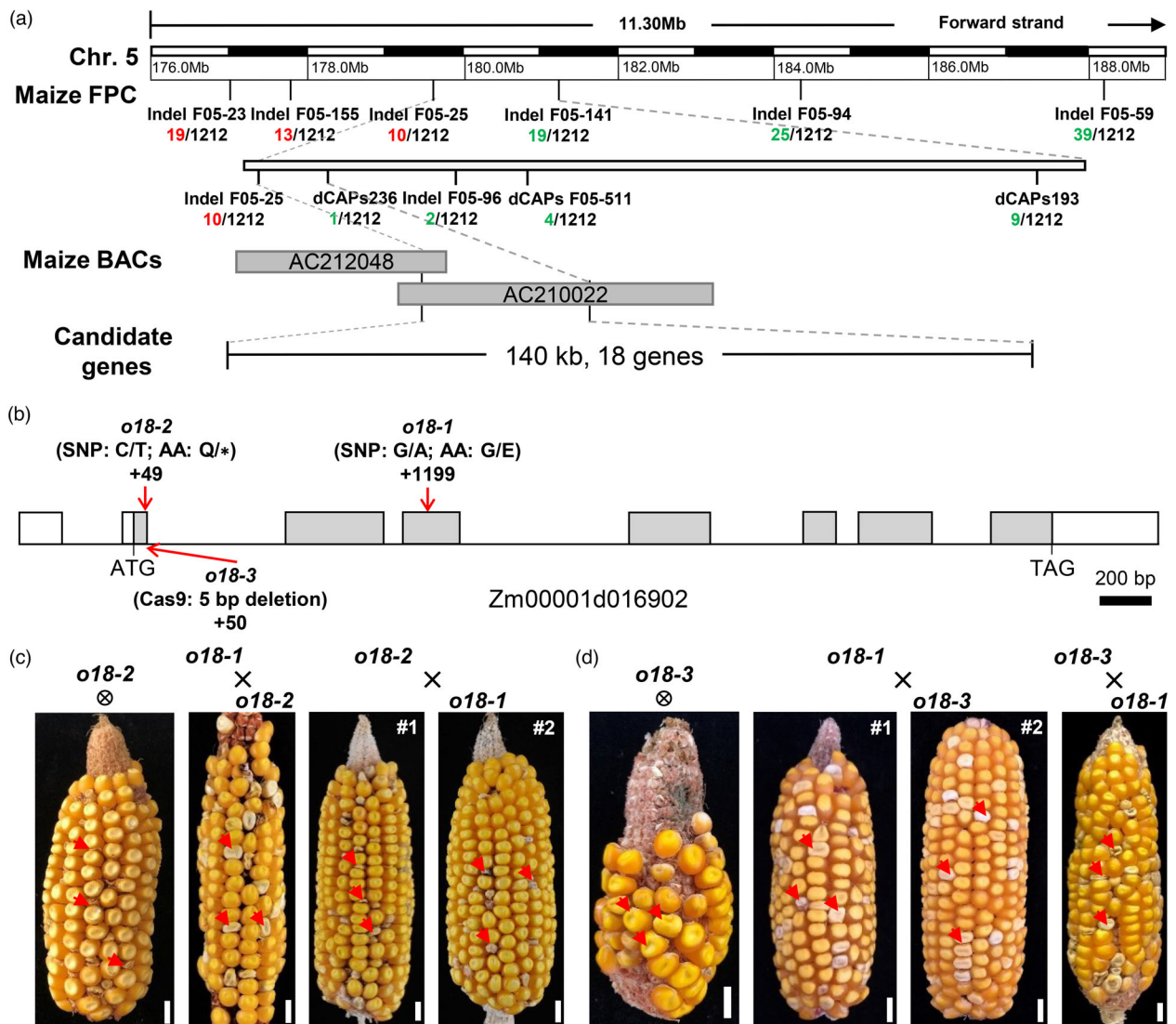


Figure 3 Map-based cloning and genetic confirmation of *O18*. (a) The *o18* locus was mapped to a 140-kb region on chromosome 5. The number under each molecular marker indicates recombinants found in the population. BAC means bacterial artificial chromosome, which represents the physical interval of *o18*. (b) Schematic diagram of the *O18* gene with indicated mutation sites. Lines represent introns, grey boxes represent coding region, and white boxes represent the 5' and 3' untranslated regions. (c) An allelism test between *o18-1* and *o18-2*. Self-pollinated ear of heterozygous *o18-2* and the reciprocally crossed ears between heterozygous *o18-1* and *o18-2* segregate defective kernels (red arrow) at a ratio of ~25%. Bar is 1 cm. (d) An allelism test between *o18-1* and *o18-3*. Self-pollinated ear of heterozygous *o18-3* and the reciprocally crossed ears between heterozygous *o18-1* and *o18-3* segregate defective kernels (red arrow) at a ratio of ~25%. Bar is 1 cm.

Maize *RIBA* genes undergo extensive duplication and are constitutively expressed

Analysis using the SMART programme revealed that *O18* encodes a putative bifunctional riboflavin biosynthesis enzyme ZmRIBA1, which possesses both 3,4-dihydroxy-2-butanone 4-phosphate synthase (DHBPS/RibB) and GTP cyclohydrolase II (GCH II/RibA) activities, to initiate the pathway (Bacher *et al.*, 2000). In comparison, *E. coli* has two split counterparts, *ribA* and *ribB* (Figure 4a). Phylogenetic topology showed that RIBA proteins have an ancestral origin, and are widely dispersed in plants, bacteria, and yeast, but lost in animals (Figure S5). Notably, bursts of gene duplication have occurred in plants, such as three and five paralogues present in *Arabidopsis* and maize genomes, respectively.

Sequence comparison revealed that *O18* paralogues, excluding ZmRIBA5, are all putative bifunctional enzymes with dual domains (Figure S6). Similar to *Arabidopsis* AtRIBA3, ZmRIBA4 has the same two residual changes at the ribulose-5-phosphate-binding region and one residual alteration at the conserved catalytic site (Figure S6A), which are required for the DHBPS activity (Fischer *et al.*, 2002; Hiltunen *et al.*, 2012). Intriguingly, ZmRIBA2 has a G-to-E substitution at the DHBPS domain, the same as the mutation site found in *o18-1* (Figure S6A). Also, it has one residual change at the catalytic region of the GCH II domain (Figure S6B), mirroring that in *Arabidopsis* AtRIBA2, whose activity has been lost (Hiltunen *et al.*, 2012). In addition, ZmRIBA3 has four residual changes in the zinc-binding region of GCH II domain (Figure S6B).

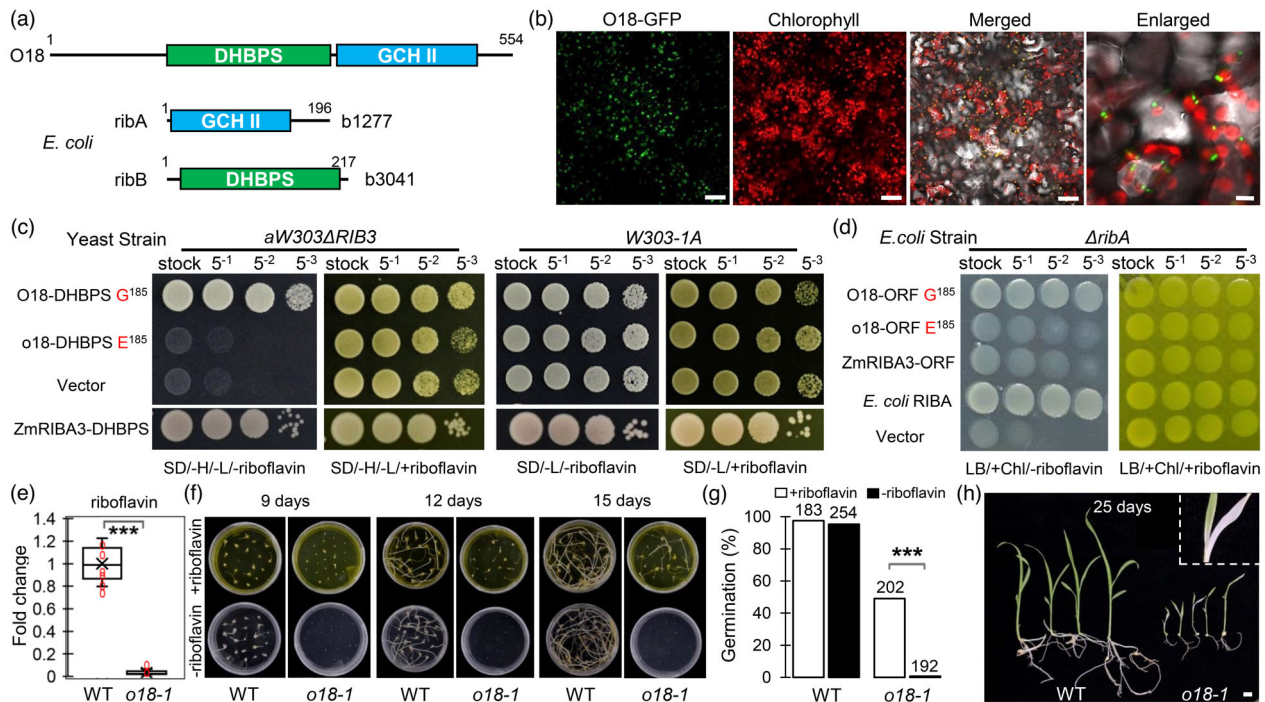


Figure 4 O18 is a plastid-localized bifunctional riboflavin biosynthesis protein ZmRIBA1. (a) Schematic diagram of maize O18 protein structure. It has a 3,4-dihydroxy-2-butanone 4-phosphate synthase (DHBPS/RibB, PF00926) and a GTP cyclohydrolase II (GCH II/RibA, PF00925) domains, in parallel to the split *E. coli* ribA and ribB. (b) O18 is targeted to chloroplast. The fusion protein O18-GFP was transiently expressed in tobacco leaf mesophyll cells. Bars are 50 μm (the first three panels) and 10 μm (the enlarged one). (c) Functional complementation of yeast mutant strain *aW303 Δ rib3* by using DHBPS domains of O18 and a paralogue ZmRIBA3. Transformants were incubated on yeast synthetic drop-out medium lacking histidine and leucine, without riboflavin (SD/-H/-L/-riboflavin) or plus riboflavin (SD/-H/-L/+riboflavin). (d) Functional complementation of *E. coli* knock-out strain BSV18 (*ribA18::Tn5*; CGSC# 6992) Δ ribA mutant by using the open reading frame (ORF) of O18 and ZmRIBA3. Transformants were incubated on LB medium containing chloramphenicol, without riboflavin (LB/+Chl/-riboflavin) or plus riboflavin (LB/+Chl/+riboflavin). (e) Riboflavin content determination in *o18-1* and the wild-type (WT) endosperm at 18 days after pollination (DAP) using HILIC LC-MS/MS analysis. For each sample, three independent biological replicates were performed. Data are means with SE (***, $P < 0.001$, two-tailed *t*-test). (f) *In vitro* riboflavin feeding assay of *o18-1*. Immature embryos were dissected from *o18-1* and WT kernels at 10 DAP, and cultured on the half MS basic medium, with or without 0.1 mM riboflavin. (g) Germination rate of embryos from *o18-1* and WT at 20 days after cultivation (DAC). Numbers above indicate the individuals used. (h) Leaf bleaching was observed in the rescued *o18-1* seedlings at 25 DAC. Bar is 1 cm.

Expression profiles using publicly available RNA-seq data showed that maize *RIBA* genes are constitutively expressed in many tissues and organs (Figure S6C). Notably, *O18/ZmRIBA1* and *ZmRIBA4* are highly expressed in developing leaves. Interestingly, *O18* and *ZmRIBA2* have a similar expression pattern, suggesting that they may function redundantly. Alternatively, it could be caused by their high sequence similarity that cannot be effectively discriminated from each other using sequencing. To ascertain the possible reason, gene-specific expression analysis revealed that *ZmRIBA2* was not expressed in any tested tissues and organs (Figure S7A). We further used a GUS reporter construct to confirm this result. As shown in Figure S7B, the *P_{ZmRIBA2}::GUS* transgenic plants showed no detectable staining signals in any tested tissues. Hence, our data revealed that *ZmRIBA2* is a *bona fide* pseudogene in maize genome.

O18 is the only RIBA enzyme possessing both GCH II and DHBPS activities for riboflavin production in maize

In line with that riboflavin is exclusively synthesized in plastids (Gerdes *et al.*, 2012), O18-GFP was colocalized with chlorophyll autofluorescence in tobacco mesophyll cells, notably forming punctuate structures in chloroplasts (Figure 4b). By using a series of Agrobacterium concentrations, we ruled out the possibility of

misfolded protein aggregates that could be caused by the strongly transient expression of O18-GFP (Figure S8).

In riboflavin biosynthesis pathway, GCH II catalyses the first step from GTP to 2,5-diamino-6-ribosylamino-4(3H)-pyrimidinone 5'-phosphate, whereas DHBPS works in the conversion from ribulose-5-phosphate into 3,4-dihydroxy-2-butanone 4-phosphate (Bacher *et al.*, 2000). We thus attempted to test the bifunctional activities of O18 and its paralogues. As expected, the DHBPS domains of O18/ZmRIBA1 and ZmRIBA3 are able to rescue the yeast counterpart mutant *Arib3* (Jin *et al.*, 2003), in contrast to failure of *o18* and ZmRIBA2 with a consensus E¹⁸⁵ (Figure 4c). Hence, the G residue at position 185 (G¹⁸⁵) is essential for the DHBPS activity of O18. Intriguingly, the complete protein, but not the GCH II domain of O18, can complement *E. coli* *AribA* mutant (Figures 4d and S9), suggesting that a physical association between the two domains is relevant to their functions. In support of this assumption, mutation of the DHBPS in *o18* inversely diminished its GCH II activity. Additionally, neither complete protein nor GCH II domain of ZmRIBA3 was able to rescue *AribA* (Figures 4d and S9). Jointly, these data revealed that O18 is the only active bifunctional RIBA protein in maize genome.

Next, we measured riboflavin content in *o18-1* developing seeds at 18 DAP, using a hydrophilic interaction liquid chromatography-tandem mass spectrometry (HILIC-LC-MS/MS)

method. As shown in Figure 4e, only around 3% of riboflavin remained in *o18-1* relative to wild type. An *in vitro* feeding assay was performed to rescue the *o18-1* embryos. Immature embryos were dissected from *o18* and wild-type seeds at 10 DAP segregated from the self-pollinated heterozygous plants, and cultured on the half MS basic medium. When supplemented with 0.1 mM riboflavin, the mutant embryos began to germinate at 9 days after cultivation (DAC), and displayed elongated shoot and root at 15 DAC (Figure 4f). In contrast, none of the *o18-1* embryos was able to grow during cultivation without riboflavin. At 20 DAC, the germination rate of *o18-1* was around 49% in the presence of riboflavin (Figure 4g), whereas no significant change in wild type with or without riboflavin. Nevertheless, the rescued *o18-1* seedlings grew slowly with some leaves having yellow-and-white variegation, when transferred into soil without supplementation of riboflavin (Figure 4h), in support of a role of riboflavin in chloroplast biogenesis (Hedtke et al., 2012).

O18 affects cellular energetics through regulating mitochondrial complex I and complex II assembly and activity

We in turn measured the contents of two riboflavin derivatives, flavin mononucleotide (FMN) and flavin adenine dinucleotide (FAD), which are essential cofactors for many metabolic reactions. The contents of FMN and FAD in *o18-1* developing seeds at 18 DAP were both reduced over 70% of that in the wild type (Figure 5a). Since they are important electron carriers, we speculated that the assembly and activity of mitochondrial respiratory complexes could be impaired in *o18-1* seeds. As shown in Figure 5b, the amount of the monomeric complex I, complex III and their supercomplex I+III was significantly decreased in *o18-1*, whereas the amount of complex V was comparable to that in wild type. Consistently, the activity of complex I was strongly impaired in the mutant (Figure 5c). Also, complex II activity was severely reduced in *o18-1* (Figure 5d), presumably due to the lack of FAD insertion into SDH1. In-gel fluorometry assay supported that the flavinylation of SDH1 and the other two mitochondrial flavoproteins was decreased upon riboflavin deficiency in *o18-1* (Figure 5e). Immunoblotting further confirmed that the abundance of subunits of complex I, II and III was drastically decreased in *o18-1* mutant, in contrast to the comparable levels of complex IV and V (Figure 5f). In line with these data, the mutant mitochondria were structurally disrupted and vacuolized, accompanied by unrecognized cristae, in developing endosperm cells (Figure 5g,h). Hence, riboflavin, as a precursor of FMN and FAD, is required for the assembly, stability and function of the monomeric complex I, II and supercomplex I+III.

Next, a targeted metabolic assay was performed to monitor the alterations of endosperm cell energetic metabolism upon riboflavin depletion. Consistent with impaired mitochondrial function, many metabolites of the tricarboxylic acid (TCA) cycle were over-accumulated in *o18-1*, which are indicative of TCA cycle perturbation (Figure 5i). Consequently, it led to decreased NADH oxidation and increased NADH/NAD⁺ ratio in *o18-1* (Figure 5j). Concomitantly, levels of several intermediates of the early and the late steps in glycolysis were drastically increased in *o18-1* relative to the wild type, in contrast to the reduced levels of intermediates of the middle reactions (Figure 5k). Finally, both lactate and acetyl-CoA were over produced in *o18-1*, indicating enhanced glycolytic flux due to mitochondrial dysfunction. Nevertheless, it was not able to fully compensate the energy loss, as illustrated by a decrease of cellular ATP production in *o18-1* (Figure 5l).

O18 modulates endosperm cell-cycle progression probably through integration of genetic and epigenetic mechanisms

Transcriptomic analysis identified 1 201 differentially expressed genes (DEGs) in endosperm at 18 DAP between *o18-1* and the wild type. Among them, 886 DEGs were functionally classified into eight categories (Figure S10A). Like the case of maize *dek33* mutant that encodes an orthologue of bacterial RibD (Dai et al., 2019), up-regulated genes in *o18-1* were also enriched in nucleosome assembly, particularly histone genes. Quantitative RT-PCR assays revealed that these histone genes were also highly expressed in *o18-1* at 15 DAP, in comparison with no difference at 10 DAP (Figure S10B). These data implied a possible cell-cycle disturbance in *o18-1* endosperm.

Next, flow cytometric assay was carried out to monitor cell proliferation and endoreduplication during endosperm development. At the mitotic stage (7 DAP), the proportion of cells in the G1 and S phases were both significantly increased in *o18-1* (Figure 6a). Endoreduplication extensively occurred in the wild-type endosperm cells at 10 DAP, as evidenced by increased proportion of higher ploidy nuclei (Figure 6b). By comparison, it was drastically reduced in *o18-1*, concomitantly with an increase in 6C and 12C levels, but a decrease in the much higher ploidy nuclei. Intriguingly, the expression of genes encoding histones, cyclins and cyclin-dependent kinases (CDKs) was highly induced in the mutant at 15 DAP (Figure 6c), favouring the existence of a negative feedback circuit in controlling cell-cycle gene transcription (Bertoli et al., 2013). Nevertheless, immunoblotting assays revealed that the levels of CDKA;1 and retinoblastoma-related1 (RBR1) were both significantly reduced in *o18-1*, relative to the wild type (Figure 6d). In agreement, the expression of DNA replication factors, like *PROLIFERATING CELL NUCLEAR ANTIGEN* and *MINICHROMOSOME MAINTENANCE* genes, which are negatively regulated by RBR1, was increased in the mutant (Figure S11). Jointly, our data revealed that riboflavin is essential for both the mitotic and endoreduplication cell-cycle regulation in maize endosperm, through the canonical cyclin D-CDKA;1-RBR1 pathway (Salazar-Roa and Malumbres, 2017).

As illustrated, human lysine-specific demethylase 1 (LSD1), an FAD-binding protein, is required for cell-cycle progression through demethylating histone H3 at lysine 4 (H3K4) (Kozub et al., 2017; Zhang et al., 2013). We investigated whether H3K4 methylation is associated with cell-cycle control in the FAD-deficient *o18-1*. Immunoblot analysis revealed that H3K4 trimethylation (H3K4me3) was over accumulated in *o18-1* (Figure 6e), which was most likely caused by functional impairment of LSD1-like proteins in maize (Figure S12). To ascertain whether increased H3K4me3 levels contribute to gene up-regulation, chromatin immunoprecipitation followed by qPCR (ChIP-qPCR) method was used to determine H3K4me3-status in cell cycle-related genes. Compared with the steady state of *Actin*, *o18-1* showed higher enrichment of H3K4me3 than the wild type at histone and cyclin genes (Figure 6f). Hence, increased H3K4me3 accounts for the induction of cell-cycle genes in *o18*, likely due to the functional impairment of H3K4me3 demethylases.

Natural variations at residue G¹⁸⁵ in *RIBA* genes and its roles in riboflavin production and osmotic stress

As aforementioned, the residue G¹⁸⁵ of O18 is essential for DHBPS activity, allowing us to assume that this locus could be highly conserved during evolution. We comprehensively

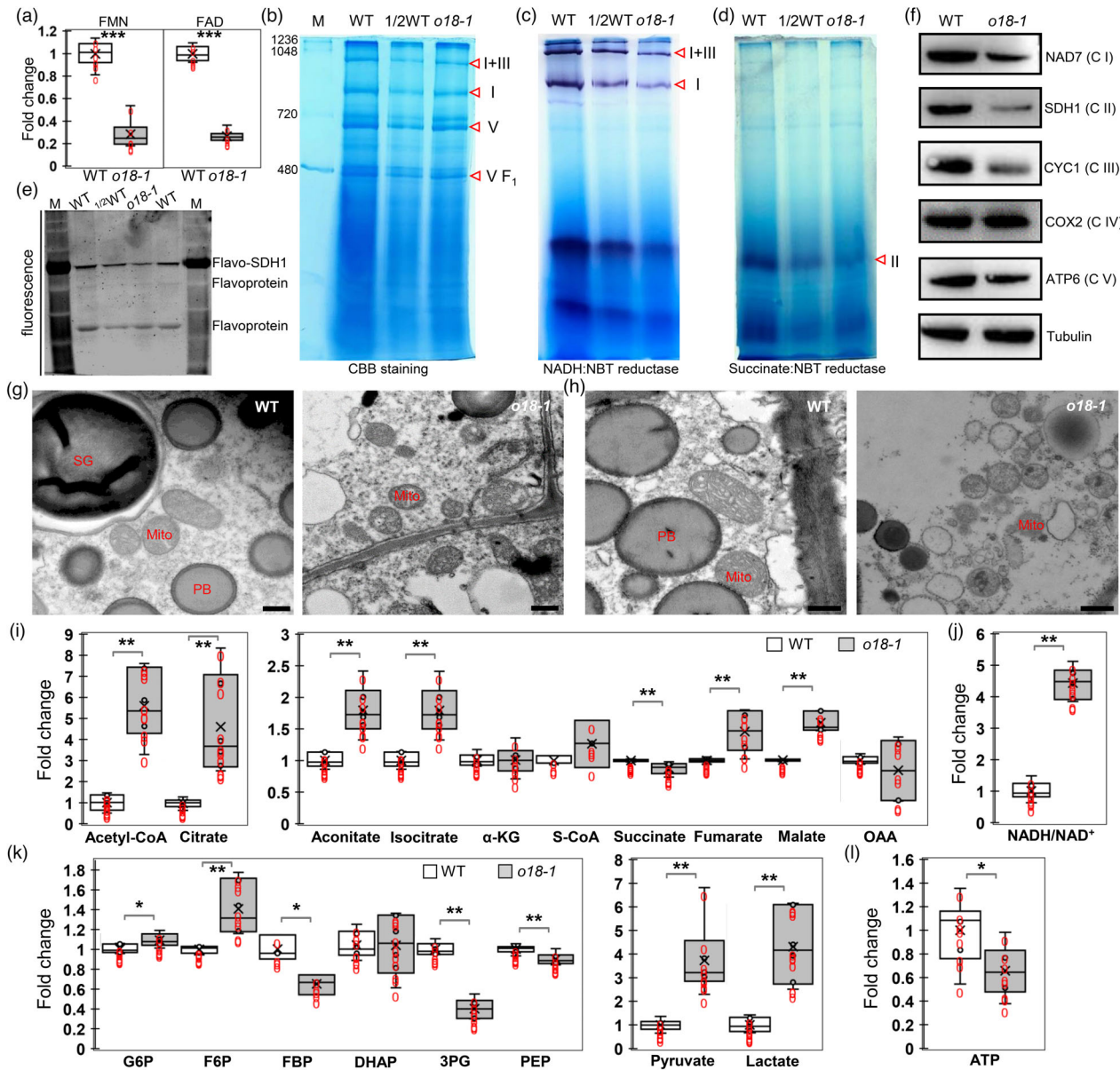


Figure 5 O18 affects the assembly and stability of complex I and complex II, and cellular energetics. (a) FMN and FAD content determination in *o18-1* and the wild-type (WT) endosperm at 18 days after pollination (DAP) using HILIC LC-MS/MS analysis. For each sample, three independent biological replicates were performed. Data are means with SE (***, $P < 0.001$, two-tailed t -test). (b) Blue native (BN) PAGE analysis of mitochondrial complexes in *o18-1*. Mitochondria from endosperm of maize developing seeds at 15 days after pollination (DAP) were loaded onto a 5% to 13.5% gradient gel, and detected by using Coomassie Brilliant Blue (CBB) staining. Red triangles indicate the corresponding mitochondrial complexes. (c) NADH dehydrogenase activity detection of complex I in *o18-1*. (d) Succinate dehydrogenase activity detection of complex II in *o18-1*. (e) In-gel fluorimetry assay of WT and *o18-1* mitochondria for covalent FAD detection. Mitochondria were resolved by 10% SDS-PAGE, incubated for 1 h in 10% acetic acid, and detected on an UV-transilluminator system. (f) Immunodetection of the representative mitochondrial proteins. Proteins were extracted from developing seeds at 18 DAP without pericarp. NAD7, SDH1, CYC1, COX2 and ATP6 are subunits of complex I, II, III, IV and V respectively. Tubulin was used as the loading control. (g, h) Ultrastructure of mitochondria in WT and *o18-1* endosperm at 15 DAP (g) and 20 DAP (h). Bar is 500 nm. (i) Comparison of metabolites involved in tricarboxylic acid (TCA) cycle in WT and *o18-1*. (j) NADH/NAD⁺ ratio in WT and *o18-1*. (k) Comparison of metabolites involved in glycolysis in WT and *o18-1*. (l) ATP levels in WT and *o18-1*. For each sample, three independent biological replicates were performed. Data are means with SE (* $P < 0.05$, ** $P < 0.01$, *** $P < 0.001$ by two-tailed t -test).

compared all available DHBPS protein sequences from bacteria, archaea, and eucarya. Equivalent to G⁶² of *E. coli* ribB, another four variations were unexpectedly observed at this residue (Figure 7a). In addition to G, residue A is found in bacteria and archaea lineages, whereas in eucarya, this locus is variable, with

three kinds of new substitutions (S, C and T). We in turn generated the four point-mutated versions in backbone of O18 DHBPS domain and transformed into yeast *Arib3* mutant. In contrast to the empty control, all of them were able to confer full complementation (Figure 7b). These data supported the notion

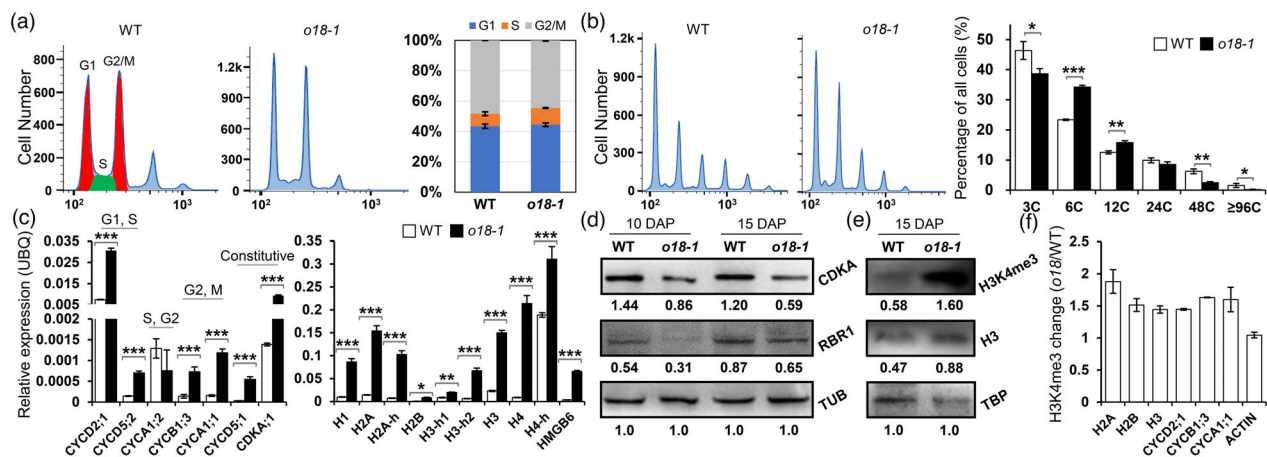


Figure 6 O18 modulates endosperm mitotic and endoreduplicating cell-cycle progression. (a) Flow cytometric assay of the mitotic cell cycle in endosperm of the wild type (WT) and *o18-1* at 7 days after pollination (DAP). Cell-cycle phases were divided as previously reported (Manthey *et al.*, 2006), in which 3C and 6C represent G1 and G2/M, while profile between them is S phase. Quantification was shown in the right panel. For each sample, three independent biological replicates were performed. (b) Flow cytometric assay of the endoreduplicating cell cycle in endosperm of the wild type (WT) and *o18-1* at 10 days after pollination (DAP). Quantification was shown in the right panel. For each sample, three independent biological replicates were performed. Data are means with SE (* $P < 0.05$, ** $P < 0.01$, *** $P < 0.001$ by student *t*-test). (c) Expression levels of cell cycle-related genes in WT and *o18-1* kernels at 15 DAP. For each RNA sample, three technical replicates were performed. Representative results from three biological replicates are shown. Error bars represent SE (*** $P < 0.001$ by student *t*-test). Transcript abundance is indicated relative to the internal control *Ubiquitin* (*UBQ*). (d) Immunodetection of CDKA and RBR1 levels in WT and *o18-1* kernels at 10 and 15 DAP. Tubulin (TUB) was used as the loading control. Quantification was performed by using the band grey intensity, relative to TUB. Representative results from three biological replicates are shown. (e) Immunodetection of H3K4me3 levels in WT and *o18-1* kernels at 15 DAP. TATA-binding protein (TBP) was used as the loading control. Quantification was performed by using the band grey intensity, relative to TBP. Representative results from three biological replicates are shown. (f) Relative H3K4me3 levels in representative genes in WT and *o18-1* kernels at 15 DAP. ChIP values were normalized to their respective DNA input values, and the fold changes were calculated based on the relative enrichment in anti-H3 compared with anti-H3K4me3 immunoprecipitates. Representative results from three biological replicates are shown.

that riboflavin biosynthetic pathway evolves independently in diverse species, after inherited from the common ancestor (Fischer and Bacher, 2011).

Intriguingly, down-regulation of Arabidopsis *AtRIBA1* leads to bleaching of leaves (Hiltunen *et al.*, 2012), and a knockout mutant *rfd1*, which was caused by transcriptional interference, is viable and forms pale green leaves (Hedtke *et al.*, 2012). The mild phenotypes appear to contradict the fact that *AtRIBA1* is the only active bifunctional enzyme for riboflavin biosynthesis in Arabidopsis (Hiltunen *et al.*, 2012). To figure out this discrepancy, CRISPR-Cas9 method was used to make knockout mutants of *AtRIBA1*. As shown in Figure 7c, four edited alleles were obtained. Of note, *atriba1-1* and *atriba1-3* both had 1-bp insertion, which gave rise to frame-shift mutations. Aborted seeds were observed from the heterozygous knockout mutants at a ratio of ~25% (Figure 7d). Therefore, *RIBA* genes play a conserved role in both monocot and dicot seed development.

As proposed that B vitamin deficiency is related to plant abiotic stress responses (Hanson *et al.*, 2016), we evaluated this hypothesis through overexpression of *O18* in transgenic Arabidopsis plants. Consistent with subcellular localization in tobacco, *O18*-GFP was targeted to chloroplasts in leaves and plastids in roots respectively (Figure 7e). The amount of riboflavin content in *O18* overexpressors was indeed increased over 30% than that in the wild type (Figure 7f), which is in line with the notion that GCH II is the rate-limiting enzyme of the pathway (Sa *et al.*, 2016).

Next, the growth of *O18* overexpressors was investigated under abiotic stresses. First, mannitol was added into half MS medium to mimic drought stress. Compared to the control, roots of *O18* overexpressors were less sensitive to osmotic stress

(Figure 7g). When grown in medium having 150 mM mannitol, the average root length of *35S::O18-GFP* transgenic lines was about 4.18 cm, which was two-fold that of WT plants (Figure 7h). This is consistent with that riboflavin accumulation can drastically enhance drought tolerance, through clearing reactive oxygen species (ROS) to keep cellular redox homeostasis that is conserved in plants and animals (Ashoori and Saedisomeolia, 2014; Deng *et al.*, 2014). Furthermore, we evaluated the effects of NaCl stress on the growth of transgenic plants. When 125 mM NaCl was added into the medium, there was no significant difference in seedling growth between wild type and *O18* overexpressors (Figure 7g,h). Based on these data, riboflavin overproduction appears to be able to counteract osmotic, but not salt stress.

Discussion

Here, we reported that *O18* is required for producing riboflavin that integrates mitochondrial energy metabolism and endosperm cell-cycle progression to control maize seed development. *O18* encodes a putative dual functional GCH II-DHBPS enzyme that catalyses the first step of riboflavin biosynthesis pathway in plastid and chloroplast in plants (Figures 4a,b, 7e and S8). Enzymatic activity of DHBPS is about two-fold that of GCH II in Arabidopsis (Herz *et al.*, 2000), guaranteeing a balanced substrate input of two molecules of ribulose phosphate and one of GTP (Bacher *et al.*, 2000). In comparison, bacteria use an FMN riboswitch to coordinate the expression of the split GCH II and DHBPS, as well as the rest riboflavin biosynthesis proteins, in a feedback manner (Garcia-Angulo, 2017), thus keeping cellular homeostasis of riboflavin. However, this barrier can be bypassed by RibR in

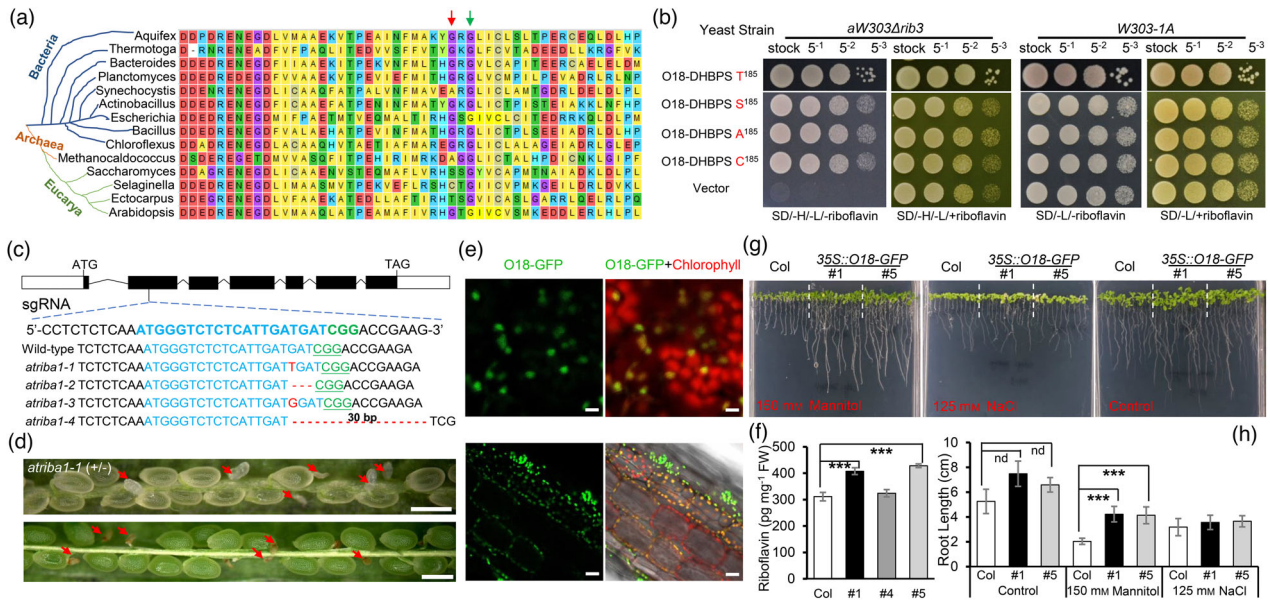


Figure 7 Natural variations at residue G¹⁸⁵ and functional analysis of *O18* for DHBPS activity, riboflavin production and stress tolerance. (a) Four types of residue substitutions detected in G¹⁸⁵ of *O18* homologues in bacteria, archaea and eukarya. G¹⁸⁵ of *O18* is equivalent to G⁶² of *E. coli* ribB (Red arrow), which is next to a conserved residue G¹⁸⁷ (G⁶⁴ of *E. coli*, Green arrow). (b) Functional complementation of yeast mutant strain *aW303Δrib3* by using DHBPS domain of *O18* having residue substitutions at G¹⁸⁵. Transformants were incubated on yeast synthetic drop-out medium lacking histidine and leucine, without riboflavin (SD/-H/-L/-riboflavin) or plus riboflavin (SD/-H/-L/+riboflavin). (c) DNA sequence identification of the CRISPR/Cas9-edited *Arabidopsis atriba1* alleles. A single-guide RNA (sgRNA) is designed in exon 2, and four alleles are obtained. The box marks exon and the dark box marks the coding region. (d) Seed phenotypes of heterozygous *atrib1-1 (+/-)* mutant. Red arrow shows the aborted homozygous seeds. (e) The fusion protein *O18*-GFP was localized in leaf chloroplast and root plastid. Bar (Upper) is 5 μm. Bar (Lower) is 20 μm. (f) Riboflavin content determination in leaves of *O18* overexpressors using HPLC with standard analysis. For each sample, three independent biological replicates were performed. Data are means with SE (***, $P < 0.001$, two-tailed t -test). (g) and (h) Osmotic and salt effects on the growth of Col-0 and 35S::*O18*-GFP seedlings. After 96 h of stratification, seeds were grown in a half MS plate for 5 days, and then transferred to medium containing 150 mM mannitol and 125 mM NaCl for an additional 7 days growth in a vertical plate. Error bars represent the standard errors of c. 100 seeds from three independent experiments (***, $P < 0.001$, two-tailed t -test). [Correction added on 6 June 2022, after first online publication: Rib3 mutant background in part label 7b is corrected in this version].

Bacillus subtilis (Pedroli *et al.*, 2015), making it an efficient system for riboflavin production. Like that in *Arabidopsis* (Hiltunen *et al.*, 2012), *O18*/ZmRIBA1 is the only active bifunctional enzyme of the five paralogues in maize genome (Figures 4c,d, 5S–S7 and 59), which is consistent with that disruption of *O18* nearly completely blocks riboflavin accumulation in maize seeds (Figure 4e). However, the roles of two monofunctional ZmRIBA3 and ZmRIBA4 remain elusive, probably counteracting each other sterically as illustrated by failure to rescue *o18* mutants. Alternatively, the monofunctional paralogues possess divergent functions, thus providing adaptive benefits to buffering under certain conditions (Garcia-Angulo, 2017; Moore, 2004).

Several essential residues have been identified in both GCH II and DHBPS domains of RIBA proteins (Fischer and Bacher, 2011; Fischer *et al.*, 2002; Hiltunen *et al.*, 2012). Here, we characterized a new site G¹⁸⁵ of *O18* (equivalent to G⁶² of *E. coli* ribB) that is required for DHBPS activity. Unexpectedly, residues at this locus appear not conserved in different species (Figure 7a,b). The crystal structure of *E. coli* ribB has revealed that this site is at the end of helix α 2 connecting to a conserved reverse turn residue G⁶⁴, residues at which are usually neutral, polar amino acids that are possibly required for generating torsion angles (Liao *et al.*, 2001). Nevertheless, their exact structural roles remain puzzling as the opposite helix propensities of G and A residues (Baldwin, 1995).

Indeed, loss of function of *O18* nearly abolishes *de novo* synthesis of riboflavin and its derivatives, FMN and FAD (Figures 4e and 5a). As the key factors of mitochondrial electron

transfer chain, FMN and FAD are pivotal for ATP generation and metabolic homeostasis. In line with that FMN is noncovalently bound to NDUFV1/NUOF, serving as an electron converter from NADH onto iron-sulphur clusters (Brandt, 2006), the amount of NADH was over accumulated in *o18-1* (Figure 5j). By contrast, FAD is covalently bound to SDH1/SDHA, mediating its maturation and the subsequent succinate oxidation of complex II (Sharma *et al.*, 2019). Consistently, flavinylation and the final amount of SDH1 are both severely reduced in *o18-1* (Figure 5e,f). Intriguingly, riboflavin itself is a component of the Na⁺-pumping NADH-quinone oxidoreductase (Na⁺-NQR) in *Vibrio cholerae* (Barquera *et al.*, 2002), but not of the mitochondrial-type H⁺-NQR.

Concomitantly, FAD can act as a cofactor for flavoproteins involved in the assembly of complex I. Acyl-CoA dehydrogenase 9 (ACAD9), an FAD-binding protein, possesses conserved activity to catalyse α - β -dehydrogenation of acyl-CoA esters, contributing to β -oxidation of fatty acids (Nouws *et al.*, 2010). Importantly, ACAD9 is a core member of the mitochondrial complex I intermediate assembly (MCIA) complex that is essential for building the intermediate ND2-module (Formosa *et al.*, 2020). Likewise, FAD-dependent oxidoreductase-containing domain 1 (FOXRED1) is not only involved in assembly of ND1-module but also links ND1 and ND2 modules probably through its interaction with ACAD9 (Rendon *et al.*, 2016). This could account for the defects in both amount and activity of holo complex I observed in the mutant (Figure 5b,c). In support of that flavinylation of SDH1 is essential for assembling complex II (Hao *et al.*, 2009), its activity

is strongly decreased in *o18-1* (Figure 5d). As illustrated by a close correlation between the decreased amount of SDH1 protein and the impaired activity of complex II (Figure 5e,f), it suggested that the non-flavinylated SDH1 appears unstable in plants. Moreover, the cellular bioenergetics shift towards aerobic glycolysis in response to mitochondrial dysfunction in *o18-1* (Figure 5i–l), which is analogous to that observed in cancer cell growth (Lunt and Heiden, 2011).

Of note, mitochondrial activity and energy reservoir is associated with the regulation of cell cycle and vice versa. We indeed observed the accumulation of cells in the G1 and S phases in the mitotic stage *o18-1* endosperm (Figure 6a), which is consistent with that disruption of either complex I activity or flavin-containing oxidases leads to G1 arrest, by sensing AMP and reactive oxygen species (ROS) as independent signalling molecules to monitor cell-cycle progression (Manthey et al., 2006; Owusu-Ansah et al., 2008; Venkatachalam et al., 2008). This also accounts for reduced endoreduplication in *o18-1* endosperm cells (Figure 6b). In maize, the canonical cyclin-dependent kinases CDKA;1/Retinoblastoma-related RBR1 pathway is required for endosperm endoreduplication. An endosperm-specific dominant negative mutant of CDKA;1 strongly suppresses endoreduplication, but not cell size, indicating that CDKA;1 plays a role in G1/S transition (Leiva-Neto et al., 2004). It is generally analogous to that observed in *o18* (Figure 6d) and some other mitochondrial dysfunction-related maize seed mutants (Dai et al., 2019; Wang et al., 2017). Moreover, knockdown of RBR1, a putative target of CDKA;1, enhances both the mitotic and endoreduplication cell cycles, but is accompanied by an unexpected reduction in cell and nuclear sizes (Sabelli et al., 2013). The genetic data confirmed that RBR1 is downstream of CDKA;1. Thus, phosphorylation of RBR1 by CDKA;1 promotes the S phase entry in cell cycle. However, the inhibitory effect of RBR1 on its related E2F targets is not enhanced in maize *cdka;1* mutant (Sabelli et al., 2013). Conversely, in Arabidopsis, these RBR1 targets are indeed down-regulated in *cdka;1* relative to the wild type (Nowack et al., 2012). Presumably, mitochondrial dysfunction in *o18* could impair phosphorylation of RBR1 by CDKA;1, in an ATP-dependent manner. Thus, it will be interesting to determine the genetic relationship between *O18* and CDKA;1.

The contrasting up-regulation of some downstream DNA replication factors in *o18* (Figure S11), however, suggests that other routes are involved in G1/S transition. This functional compensation could be partially explained by extensive duplication of cyclins, CDKs and E2Fs in higher organisms (Bertoli et al., 2013). Notably, retinoblastoma (RB) loss in some human and mouse tissues decreases mitochondrial mass and function, which has been proposed to be stemmed from mitophagy (Nicolay et al., 2015). In contrast, increased mitochondrial cytochrome c in maize *rbr1* is indicative of endosperm programmed cell death (PCD), other than mitochondrial damage (Sabelli et al., 2013). Intriguingly, CDK4/6 inhibition in human cells leads to increased mitochondrial accumulation and enhanced respiratory function, which is dependent on RB (Franco et al., 2016). Whether this scenario is conserved in plants deserves to be further investigated.

In parallel, mitochondrial defects and lack of ATP can prevent cell-cycle progression in either G1/S or G2/M transitions, by suppressing cell cycle-related genes (Salazar-Roa and Malumbres, 2017). Nonetheless, the unexpected up-regulation of cell-cycle genes in *o18* suggests additional machinery implicated in cell-cycle control. Indeed, LSD1-mediated H3K4 methylation regulates cell-cycle progression in various tumours (Kozub et al., 2017). As FAD is an essential cofactor for H3K4 demethylase of LSD1-like

proteins (Hino et al., 2012), we observed H3K4me3 enrichment and the resulting up-regulation of cell-cycle genes in *o18* (Figure 6c–f), which is lack of FAD. In cancer cells, LSD1 directly methylases and represses myosin phosphatase target subunit 1 (MYPT1), which inhibits dephosphorylation of RB1 and promotes cell-cycle progression (Cho et al., 2011). Moreover, human herpes simplex virus host cell factor-1 (HCF1) recruits trithorax-related mixed-lineage leukaemia (MLL) and Set1 for H3K4me3 deposition on E2F-responsive promoters, leading to transcriptional activation and G1/S transition (Tyagi et al., 2007). Besides, LSD1 can manipulate the expression of regulators of energy expenditure and mitochondrial metabolism to maintain cellular energetics, in an FAD-dependent H3K4 demethylation manner (Hino et al., 2012). It should be pointed out that this activation cannot bypass the cell-cycle arrest in *o18*, but provides a possible epigenetic control for cell-cycle progression.

In summary, our study demonstrates a comprehensive scenario of mutual connections and coordinated adaptation among nutrients, like vitamin B₂, cellular energy, and cell cycle, in three different cell compartments (Figure S13). In plant cells, VB₂ is *de novo* synthesized in plastid through an evolutionarily conserved pathway that is composed of nuclear-encoded proteins. The subsequent FMN and FAD are synthesized in either plastid, cytoplasm, or mitochondrion. In line with the dominant roles in redox reactions, FMN and FAD primarily act as electron carriers, coupling to proton generation in mitochondrial complex I and complex II. Importantly, as a cofactor, FAD decorates several proteins that are required for assembly, maturation and stability of respiratory complexes. Mitochondrial energy thus fuels the G1/S transition in both mitotic and endoreduplicating endosperm cell cycles, in a canonical cyclin D-CDKA-RBR-E2F-dependent fashion. Conversely, mutation of *O18* abolishes the biosynthesis of VB₂ and the two derivatives, FMN and FAD. It consequently impairs cellular energetics by disrupting mitochondrial complex I and complex II assembly and activity. The strong deprivation of cellular energy leads to G1 and S phases arrest of endosperm cells, by undermining either CDKA activity or triggering specific cell-cycle checkpoints. The unexpected inducing of cell-cycle genes in *o18* is associated with the increase of H3K4me3 modification in them, which is probably accounted by dysfunction of FAD-dependent LSD1-like proteins. This induction cannot reverse cell-cycle defects, but indeed evidences an epigenetic control of cell cycle. Thus, we propose that this H3K4 methylation-mediated regulation may be a back-up mechanism of cell-cycle progression in nutrient-deficient and energy-insufficient adaptation.

Materials and methods

Plant materials and growth conditions

The maize (*Zea mays* L.) mutant 3605K (dnj*-N1534, *o18-1*) was obtained from the Maize Genetics Cooperation stock centre (<http://maizecoop.crops.corn.edu/>), and an EMS-generated Stop-Gained mutant (EMS3-05e806, *o18-2*, Q49*) was obtained from Maize EMS induced Mutant Database (MEMD) (<http://www.elabcaas.cn/memd/>). *o18-1* was crossed into the W64A inbred line, and The F₁ heterozygous plants (*o18-1/+*) were self-crossed to generate a F₂ mapping population. The maize materials were planted in the field at Shanghai (China), Zhongmou (Zhengzhou, China), and Sanya (Hainan, China), in growing season.

Root, stem, leaf, silk, tassel, and ear tissues were harvested from W22 at the V12 stage (Wang et al., 2010). Endosperm, embryo and pericarp were also dissected from kernels of W22 as

described before (Ni *et al.*, 2019). Tobacco (*Nicotiana benthamiana* L.) was grown in a growth chamber under long day conditions (16 h light, 8 h dark, 25 °C). The *Arabidopsis thaliana* (L.) ecotype Colombia (Col-0) was used as the WT. Seeds were germinated and grown on half MS medium (PhytoTech LABS, Shawnee Mission, USA) plates containing 0.8% agar and 1% sucrose. After 3-days of stratification at 4 °C, plates were placed in a growth chamber under long day conditions (16 h light, 8 h dark, 22 °C). For mannitol treatment, seeds were grown in a vertical position for 4 days on half MS medium, and then transferred to medium containing various concentrations of mannitol for an additional 8 days of vertical growth. For NaCl treatment, seeds were germinated and grown in medium containing various concentrations of NaCl for 10 days.

Measurements of starch and proteins in seeds

Mature kernels of *o18-1* and the wild type were collected from the middle region of the well-filled and self-crossed heterozygous ears. After removing embryo and pericarp parts, endosperm samples were fine powdered in liquid nitrogen and further dried to constant weight. Total proteins, zein, and nonzein were extracted from 50 mg of three pooled endosperm flour samples as previously described (Wang *et al.*, 2011). Protein content was measured using a Pierce™ BCA standard kit (Thermo Fisher Scientific, Waltham, USA). Measurements of all samples were replicated three times. SDS-PAGE was performed in 12% polyacrylamide gels, and the gels were stained with Coomassie brilliant blue R250. For starch measurements, an amyloglucosidase/ α -amylase starch assay kit (Megazyme, Wicklow, Ireland) was used according to the manufacturer's protocol.

Light microscopy and transmission electron microscopy

For paraffin sections, developing kernels of *o18-1* and the wild type were collected from the same segregating ears of self-crossed heterozygous plants. Samples were sliced along the longitudinal axis into three equal parts and the middle one was used, as the method described before (Wang *et al.*, 2019). For transmission electron microscopy, developing kernels of *o18-1* and the wild type were implemented according to the methods described previously (Wang *et al.*, 2012a).

Plasmid construction and the CRISPR/Cas9 Mutagenesis

To generate the overexpression construct *UBQ::O18*, the coding sequences of *O18* minus the stop codon were amplified from cDNA of W22 developing kernels using primers listed in Extended Table S1. The resulting product was cloned into pENTR/D-TOPO (Invitrogen, USA), followed by clonase reaction with the modified binary vector pB7FWG2.0 having a maize *UBQ* promoter.

For CRISPR/Cas9 gene-editing assay, two sgRNAs 5'-CA AAGACACGCAACTTTGGTAGG-3' and 5'-AGCAGCTTCTTACGG TTGACGGG-3' were designed and driven by a maize *U6* promoter, thus incorporated into *pCPB-ZmUbi-hspCas9* as a single-sgRNA vector, respectively, as instructed previously (Liu *et al.*, 2020).

The resulting constructs were transformed into the KN5585 inbred line immature zygotic embryos through the *Agrobacterium*-mediated method. Stable T₁ and later-generation individuals were used for further analysis.

Map-based cloning

The *o18* locus was mapped using 1,212 mutant individuals from an F₂ segregating population derived from the self-pollinated F₁ (W64A \times *o18/+*) plants. Preliminary mapping was carried out using

the polymorphic InDel markers distributed throughout maize ten chromosomes. For fine mapping, molecular markers on chromosome 5 were developed and used to narrow the *o18* locus to a 140-kb interval between markers InDel F05-25 and dCAPs236, as listed in Extended Table S1. This region contains 18 annotated genes according to maize B73_RefGen_v4. cDNA and DNA fragments of the candidate genes were amplified from the mutant and wild-type plants using KOD PLUS DNA polymerase (TOYOBO, Japan) and further sequenced.

Functional complementation of yeast strain *Arib3*

For functional complementation experiments, an yeast *RIB3* mutant strain (*aW303Arib3*) (Jin *et al.*, 2003), in which a single base mutation results in an amino acid substitution (A137T), and wild-type *W303-1A* strain were kindly provided by Dr. Tzagoloff as a gift. The mutant strain was cultured and kept in YPDA medium containing 25 μ g/mL riboflavin.

The cDNA fragments, encoding for DHBPS domains, of *O18/ZmRIBA1*, *ZmRIBA2*, *ZmRIBA3* and mutated *O18*, were cloned into the pMD18-T vector, using primers listed in Extended Table S1. After sequencing, the plasmid fragments were ligated into a modified pNH605 vector with an *ADH* promoter, by using double digests with *Xho* I and *Bam*HI. The resulting constructs were transformed into *aW303Arib3* and *W303-1A* strains using a standard procedure.

Embryo rescue assay

Immature kernels of *o18-1* and the wild type at 10 DAP were surface-sterilized in 10% H₂O₂ for 30 min, and then were rinsed with sterile water at least three times. The developing embryos were carefully taken out and cultured in MS medium (2.2 g/L MS, 40 g/L sucrose, 7 g/L agar), with or without 0.1 mM riboflavin, in a growth chamber at 25 °C, under dark condition. The germination rate of embryos was counted after 15 days of incubation.

Flow cytometry

Extraction of nuclei was carried out using a method described previously (Dolezel *et al.*, 2007; He *et al.*, 2019). Endosperm of five genotyped developing kernels of *o18-1* and the wild type was pulled from the same segregated ears at 7, 10 and 15 DAP. At least three individual ears were used for the flow cytometry analysis. The nuclei suspension was measured using an FACSCelesta flow cytometer (BD Biosciences, USA) equipped with an argon-ion laser tuned at a wavelength of 488 nm. For each sample, at least 10 000 nuclei were collected and analysed using a Flowjo software.

RNA extraction and reverse-transcription PCR

Approximately 100 mg of fresh tissues was immediately frozen in liquid nitrogen and ground into fine powder. Total RNA was extracted with Trizol reagent (Sigma, USA) according to the standard manual. First-strand cDNA was synthesized using a PrimeScript® RT Reagent Kit (TaKaRa, Japan) after the digestion of residual genomic DNA. Quantitative real-time PCR was performed using a ChamQ Universal SYBR qPCR Master Mix (Q711/02/03; Vazyme, Nanjing, China) with CFX96™ Real-Time System (Bio-Rad, USA), using primers listed in Extended Table S1. Maize *UBQ1* was used as an internal control. The specificity of the PCR amplification procedures was checked with a heat dissociation curve protocol. Transcript abundance was calculated relative to *UBQ1*.

Bioinformatical analysis

Amino acid sequences of RIBA proteins were retrieved from the Gramene database (<http://www.gramene.org>) and the Ensembl browser (<http://asia.ensembl.org/index.html>). Protein domain architecture was analysed using the SMART program (<http://smart.embl-heidelberg.de/>). Multiple sequence alignment was carried out using the Clustal Omega program (<https://www.ebi.ac.uk/Tools/msa/clustalo/>) and ESPript 3.0 (<https://esprict.ibcp.fr/ESPrict/cgi-bin/ESPrict.cgi>) with default parameters. Phylogenetic analysis was performed using the neighbour-joining method in MEGA 7 (<https://www.megasoftware.net/>) for unrooted phylogeny tree construction supported by 1000 bootstrap reiterations.

Subcellular localization

For subcellular localization, the complete coding sequence (CDS) of *O18* without stop codon was amplified from cDNA of B73 and cloned into pENTR/D-TOPO (Invitrogen), and the fidelity was verified by sequencing. The full-length CDS of *O18* was ligated into pGWB605 vector by LR-clonase reaction to generate *Pro35S::O18-GFP* construct. The resulting construct was introduced into *Agrobacterium tumefaciens* GV3101 strain and then infiltrated into tobacco (*Nicotiana benthamiana*) leaves for transient expression. After transformation for 48 h, the GFP-fused protein and chlorophyll autofluorescence were observed under a laser confocal microscope (CarlZeiss LSM710, Germany).

Mitochondrial complex activity and blue-native gel electrophoresis

Mitochondria were isolated from 0.3 g endosperm of *o18-1* and the wild type at 15DAP, using a Cytoplasmic and Mitochondrial Protein Extraction Kit (Sangon Biotech, Shanghai, China), and were analysed using Blue Native PAGE (BN-PAGE) according to a modified method (Meyer *et al.*, 2009). Briefly, mitochondria pellet was resolved in 50 μ L B25G20 solution (25 mM Bis-Tris, 20% glycerine, pH 7.0, adding 20% DDM to a final concentration of 1%) and gently mixed. After ice-bath for 1 h, the homogenate was centrifuged at 12 000 rpm for 15 min at 4 °C, and then the supernatant was collected and the loading buffer was added before BN-PAGE. The separating gel consisted of a linear gradient of 5%–13.5% (W/V) acrylamide and a stacking gel of 4% (W/V) acrylamide. Electrophoresis was carried out at 4 °C, using a first voltage of 50 V and then adding 25 V every 30 min to a final 175 V, until the loading dye migrated to the edge of the gel. The cathode buffer (50 mM Tricine, 15 mM Bis-Tris) and the anode buffer (50 mM Bis-Tris) were adjusted pH to 7.0 with HCl at 4 °C. The gel was stained by using Coomassie Brilliant blue G-250.

In-gel activity assay of mitochondrial complexes I and II after BN-PAGE was performed as previously described with some modification (Sabar *et al.*, 2005). NADH dehydrogenase activity of complex I was detected using a nitro-blue tetrazolium (NBT) staining. Briefly, the gradient gel was rinsed with distilled water, equilibrated in 20 mM Tris-HCl buffer (pH 7.4) for 5 min, and then transferred the gel in fresh 20 mM Tris-HCl buffer (pH 7.4) plus 0.1% NBT for 20 min; finally, the gel was incubated in fresh 20 mM Tris-HCl buffer (pH 7.4) plus 1 mM NADH, until enough dark blue staining. For complex II activity, the gradient gel was rinsed with distilled water, equilibrated in the reaction buffer (50 mM KH_2PO_4 , 0.2 mM PMS, 10 mM succinate, adjust pH to 7.4 and then add 0.1 mM ATP) for 10 min, and then transferred in fresh reaction buffer plus 0.2% NBT for 15–30 min until

enough dark blue staining was reached. Reaction was stopped in a fixation solution of 45% (v/v) ethanol and 10% (v/v) acetic acid. All incubation steps were carried out in a shaking table at room temperature in dark.

Total protein extraction and immunoblot assays

Mitochondrial protein of *o18-1* and the wild-type developing endosperm were separated using SDS-PAGE, and then transferred onto an NC membrane (0.22 μ m; Millipore, Germany) using a Mini-transblot system (Bio-Rad) for Western blotting with antibodies against α -Tubulin (1/5000), NAD7 (1/2000), SDH1 (1/2000), CYC1 (1/2000), COX2 (1/2000) and ATP6 (1/2000) in rabbits according to the standard protocol.

Targeted metabolomics

Endosperm of *o18-1* and the wild type at 18 DAP was collected and ground into a fine powder. Metabolites determination was performed using a targeted metabolomics service provided by Shanghai Applied Protein Technology. The LC-MS analysis was performed using ACQUITY UPLC I-Class PLUS System (Waters) coupled to AB SCIEX QTRAP 5500 mass spectrometer with an ACQUITY UPLC BEH Amide Column (130 Å, 1.7 μ m, 2.1 mm \times 100 mm).

Chromatin immunoprecipitation-quantitative PCR

The ChIP assay was performed according to a protocol described before with modifications (Li *et al.*, 2015). Briefly, 2.5 g endosperm powder was cross-linked in M1 buffer (25 mL) with 1% formaldehyde on ice for 10 min, and the reaction was stopped by adding glycine to a final concentration of 0.125 M. The homogenate was filtered through a double layer of Miracloth. Nuclear-enriched extracts were washed three times with 5 mL M2 buffer and once with M3 buffer, and resuspended into 1 mL sonication buffer. After a first sonication of 80% amplitude for 5 min with a Bioruptor UCD-200 (Diagenode), the suspension was centrifuged at 100 g to remove the residual starch. The supernatant chromatin was further sonicated for 20 min on 80% amplitude to create 150–250 bp DNA fragments. Antibodies against H3 (Sigma, #H9289) and the H3K4me3 (ABclonal A2357) were used for immunoprecipitation. The precipitated DNA was purified using a Universal DNA Purification Kit (TIANGEN Cat. #DP214-02; Beijing, China) and analysed by quantitative PCR using a ChamQ Universal SYBR qPCR Master Mix (Q711/02/03; Vazyme) with CFX96™ Real-Time System (Bio-Rad, USA). The H3K4me3 target primers were designed based on the ZEAMAP program (http://www.zeamap.com/browser/washu/?genome=B73&hub=WashU_browser/B73/hubs/Histone_Modification.json), as listed in Extend Table S1. ChIP values were normalized to their respective DNA input values, and the fold changes in concentration were calculated based on the relative enrichment in anti-H3 compared with anti-H3K4me3 immunoprecipitates. The means and standard deviations were calculated from three biological replicates.

SDH1 flavinylation assay

The flavinylation assay was carried out by a UV-transilluminator method described previously (Bafunno *et al.*, 2004). Mitochondria protein of developing endosperm at 15 DAP was separated by 10% SDS-PAGE, then the unstained gel was incubated for 1 h in 10% acetic acid and inspected on an UV-transilluminator system (Bio-Rad, USA). The fluorescence intensity was analysed using ImageJ software.

Quantification and statistical analysis

For metabolites analysis, we applied a two-tailed *t*-test in SigmaPlot 12.5. The means and SEM were derived from three independent biological samples.

Accession Numbers

Sequence data from this article can be found in the Phytozome database with the gene IDs listed in Table S2.

Funding

This research was supported by grants from the National Natural Sciences Foundation of China U1804235, the Ministry of Science and Technology of China 2021YFF1000304, and 32001562, a grant from the Natural Science Foundation of Shanghai 17ZR1409400 (to GW).

Conflict of interests

The authors declare no competing interests.

Author contributions

GFW and QT designed the experiments. GW, XM, QS, MD, XY, XL, RI, ZW, XW and ZF performed the experiments and generated the data. GFW, GW, QY and JT analysed the data. GFW and GW wrote the manuscript.

Data availability statement

All data needed to evaluate the conclusions in the paper are present in the paper and/or the Supplementary Materials. Additional data related to this paper may be requested from the authors.

References

- Ashoori, M. and Saedisomeolia, A. (2014) Riboflavin (vitamin B2) and oxidative stress: a review. *Br. J. Nutr.* **111**, 1985–1991.
- Bacher, A., Eberhardt, S., Fischer, M., Kis, K. and Richter, G. (2000) Biosynthesis of vitamin B2 (riboflavin). *Annu. Rev. Nutr.* **20**, 153–167.
- Bafunno, V., Giancaspero, T.A., Brizio, C., Bufano, D., Passarella, S., Boles, E. and Barile, M. (2004) Riboflavin uptake and FAD synthesis in *Saccharomyces cerevisiae* mitochondria: involvement of the Flx1p carrier in FAD export. *J. Biol. Chem.* **279**, 95–102.
- Balasubramaniam, S., Christodoulou, J. and Rahman, S. (2019) Disorders of riboflavin metabolism. *J. Inherit. Metab. Dis.* **42**, 608–619.
- Balasubramaniam, S. and Yapito-Lee, J. (2020) Riboflavin metabolism: role in mitochondrial function. *J. Transl. Genet. Genom.* **4**, 285–306.
- Baldwin, R.L. (1995) α -Helix formation by peptides of defined sequence. *Biophys. Chem.* **55**, 127–135.
- Barquera, B., Zhou, W.D., Morgan, J.E. and Gennis, R.B. (2002) Riboflavin is a component of the Na⁺-pumping NADH-quinone oxidoreductase from *Vibrio cholerae*. *Proc. Natl Acad. Sci. USA*, **99**, 10322–10324.
- Bertoli, C., Skotheim, J.M. and de Bruin, R.A.M. (2013) Control of cell cycle transcription during G1 and S phases. *Nat. Rev. Mol. Cell Biol.* **14**, 518–528.
- Brandt, U. (2006) Energy converting NADH: quinone oxidoreductase (Complex I). *Annu. Rev. Biochem.* **75**, 69–92.
- Cho, H.-S., Suzuki, T., Dohmae, N., Hayami, S., Unoki, M., Yoshimatsu, M., Toyokawa, G. et al. (2011) Demethylation of RB Regulator MYPT1 by histone demethylase LSD1 promotes cell cycle progression in cancer cells. *Can. Res.* **71**, 655–660.
- Dai, D., Tong, H., Cheng, L., Peng, F., Zhang, T., Qi, W. and Song, R. (2019) Maize Dek33 encodes a pyrimidine reductase in riboflavin biosynthesis that is essential for oil-body formation and ABA biosynthesis during seed development. *J. Exp. Bot.* **70**, 5173–5187.
- Deng, B., Jin, X., Yang, Y., Lin, Z. and Zhang, Y. (2014) The regulatory role of riboflavin in the drought tolerance of tobacco plants depends on ROS production. *Plant Growth Regul.* **72**, 269–277.
- Dolezel, J., Greilhuber, J. and Suda, J. (2007) Estimation of nuclear DNA content in plants using flow cytometry. *Nat. Protoc.* **2**, 2233–2244.
- Feng, F., Qi, W.W., Lv, Y.D., Yan, S.M., Xu, L.M., Yang, A.Y., Yuan, Y. et al. (2018) OPAQUE11 is a central hub of the regulatory network for maize endosperm development and nutrient metabolism. *Plant Cell*, **30**, 375–396.
- Fischer, M. and Bacher, A. (2011) Biosynthesis of vitamin B2 and flavocoenzymes in plants. In *Advances in Botanical Research* (Rébeillé, F. and Douce, R., eds), pp. 93–152. United States: Academic Press.
- Fischer, M., Römisch, W., Schiffmann, S., Kelly, M., Oschkinat, H., Steinbacher, S., Huber, R. et al. (2002) Biosynthesis of riboflavin in archaea studies on the mechanism of 3,4-dihydroxy-2-butanone-4-phosphate synthase of *Methanococcus jannaschii*. *J. Biol. Chem.* **277**, 41410–41416.
- Formosa, L.E., Muellner-Wong, L., Reljic, B., Sharpe, A.J., Jackson, T.D., Beilharz, T.H., Stojanovski, D. et al. (2020) Dissecting the roles of mitochondrial complex I intermediate assembly complex factors in the biogenesis of complex I. *Cell Rep.* **31**, 107541.
- Franco, J., Balaji, U., Freinkman, E., Witkiewicz, A.K. and Knudsen, E.S. (2016) Metabolic reprogramming of pancreatic cancer mediated by CDK4/6 inhibition elicits unique vulnerabilities. *Cell Rep.* **14**, 979–990.
- Garcia-Angulo, V.A. (2017) Overlapping riboflavin supply pathways in bacteria. *Crit. Rev. Microbiol.* **43**, 196–209.
- Gerdes, S., Lerma-Ortiz, C., Frelin, O., Seaver, S.M.D., Henry, C.S., de Crecy-Lagard, V. and Hanson, A.D. (2012) Plant B vitamin pathways and their compartmentation: a guide for the perplexed. *J. Exp. Bot.* **63**, 5379–5395.
- Gibbon, B.C. and Larkins, B.A. (2005) Molecular genetic approaches to developing quality protein maize. *Trends Genet.* **21**, 227–233.
- Hanson, A.D., Beaudoin, G.A., McCarty, D.R. and Gregory, J.F. (2016) Does abiotic stress cause functional b vitamin deficiency in plants? *Plant Physiol.* **172**, 2082–2097.
- Hao, H.X., Khalimonchuk, O., Schraders, M., Dephore, N., Bayley, J.P., Kunst, H., Devile, P. et al. (2009) SDH5, a gene required for flavination of succinate dehydrogenase, is mutated in paraganglioma. *Science*, **325**, 1139–1142.
- Hasnain, G., Frelin, O., Roje, S., Ellens, K.W., Ali, K., Guan, J.-C., Garrett, T.J. et al. (2013) Identification and characterization of the missing pyrimidine reductase in the plant riboflavin biosynthesis pathway. *Plant Physiol.* **161**, 48–56.
- He, Y., Wang, J., Qi, W. and Song, R. (2019) Maize Dek15 encodes the cohesin-loading complex subunit SCC4 and is essential for chromosome segregation and kernel development. *Plant Cell*, **31**, 465–485.
- Hedtke, B., Alawady, A., Albacete, A., Kobayashi, K., Melzer, M., Roitsch, T., Masuda, T. et al. (2012) Deficiency in riboflavin biosynthesis affects tetrapyrrole biosynthesis in etiolated *Arabidopsis* tissue. *Plant Mol. Biol.* **78**, 77–93.
- Herz, S., Eberhardt, S. and Bacher, A. (2000) Biosynthesis of riboflavin in plants. The ribA gene of *Arabidopsis thaliana* specifies a bifunctional GTP cyclohydrolase II/3,4-dihydroxy-2-butanone 4-phosphate synthase. *Phytochemistry*, **53**, 723–731.
- Hiltunen, H.M., Illarionov, B., Hedtke, B., Fischer, M. and Grimm, B. (2012) Arabidopsis RIBA proteins: two out of three isoforms have lost their bifunctional activity in riboflavin biosynthesis. *Int. J. Mol. Sci.* **13**, 14086–14105.
- Hino, S., Sakamoto, A., Nagaoka, K., Anan, K., Wang, Y., Mimasu, S., Umehara, T. et al. (2012) FAD-dependent lysine-specific demethylase-1 regulates cellular energy expenditure. *Nat. Commun.* **3**, 758.
- Jiao, Y., Peluso, P., Shi, J., Liang, T., Stitzer, M.C., Wang, B., Campbell, M.S. et al. (2017) Improved maize reference genome with single-molecule technologies. *Nature*, **546**, 524–527.
- Jin, C., Barrientos, A. and Tzagoloff, A. (2003) Yeast dihydroxybutanone phosphate synthase, an enzyme of the riboflavin biosynthetic pathway, has a second unrelated function in expression of mitochondrial respiration. *J. Biol. Chem.* **278**, 14698–14703.
- Kaelin, W.G. and McKnight, S.L. (2013) Influence of metabolism on epigenetics and disease. *Cell*, **153**, 56–69.

- Kozub, M.M., Carr, R.M., Lomber, G.L. and Fernandez-Zapico, M.E. (2017) LSD1, a double-edged sword, confers dynamic chromatin regulation but commonly promotes aberrant cell growth. *F1000Research*, **6**, 2016.
- Leiva-Neto, J.T., Grafi, G., Sabelli, P.A., Woo, Y.M., Dante, R.A., Maddock, S., Gordon-Kamm, W.J. et al. (2004) A dominant negative mutant of cyclin-dependent kinase A reduces endoreduplication but not cell size or gene expression in maize endosperm. *Plant Cell*, **16**, 1854–1869.
- Li, C., Qiao, Z., Qi, W., Wang, Q., Yuan, Y., Yang, X., Tang, Y. et al. (2015) Genome-wide characterization of cis-acting DNA targets reveals the transcriptional regulatory framework of Opaque2 in maize. *Plant Cell*, **27**, 532–545.
- Liao, D.-I., Calabrese, J.C., Wawrzak, Z., Viitanen, P.V. and Jordan, D.B. (2001) Crystal structure of 3,4-dihydroxy-2-butanone 4-phosphate synthase of riboflavin biosynthesis. *Structure*, **9**, 11–18.
- Liu, H.-J., Jian, L., Xu, J., Zhang, Q., Zhang, M., Jin, M., Peng, Y. et al. (2020) High-throughput CRISPR/Cas9 mutagenesis streamlines trait gene identification in maize. *Plant Cell*, **32**, 1397–1413.
- Lu, X., Liu, J., Ren, W., Yang, Q., Chai, Z., Chen, R., Wang, L. et al. (2018) Gene-indexed mutations in maize. *Mol. Plant*, **11**, 496–504.
- Lunt, S.Y. and Heiden, M.G.V. (2011) Aerobic glycolysis: meeting the metabolic requirements of cell proliferation. *Annu. Rev. Cell Dev. Biol.* **27**, 441–464.
- Manthey, K.C., Rodriguez-Melendez, R., Hoi, J.T. and Zemleni, J. (2006) Riboflavin deficiency causes protein and DNA damage in HepG2 cells, triggering arrest in G1 phase of the cell cycle. *J. Nutr. Biochem.* **17**, 250–256.
- Massey, V. (2000) The chemical and biological versatility of riboflavin. *Biochem. Soc. Trans.* **28**, 283–296.
- Meyer, E.H., Tomaz, T., Carroll, A.J., Estavillo, G., Delannoy, E., Tanz, S.K., Small, I.D. et al. (2009) Remodeled respiration in *ndufs4* with low phosphorylation efficiency suppresses Arabidopsis germination and growth and alters control of metabolism at night. *Plant Physiol.* **151**, 603–619.
- Moore, B.D. (2004) Bifunctional and moonlighting enzymes: lighting the way to regulatory control. *Trends Plant Sci.* **9**, 221–228.
- Myers, A.M., James, M.G., Lin, Q.H., Yi, G., Stinard, P.S., Hennen-Bierwagen, T.A. and Becraft, P.W. (2011) Maize opaque5 encodes monogalactosyldiacylglycerol synthase and specifically affects galactolipids necessary for amyloplast and chloroplast function. *Plant Cell*, **23**, 2331–2347.
- Ni, J., Ma, X., Feng, Y., Tian, Q., Wang, Y., Xu, N., Tang, J. et al. (2019) Updating and interaction of polycomb repressive complex 2 components in maize (*Zea mays*). *Planta*, **250**, 573–588.
- Nicolay, B.N., Danielian, P.S., Kottakis, F., Lapek, J.D., Sanidas, I., Miles, W.O., Dehnad, M. et al. (2015) Proteomic analysis of pRb loss highlights a signature of decreased mitochondrial oxidative phosphorylation. *Genes Dev.* **29**, 1875–1889.
- Nouws, J., Nijtmans, L., Houten, S.M., van den Brand, M., Huynen, M., Venselaar, H., Hoefs, S. et al. (2010) Acyl-CoA dehydrogenase 9 is required for the biogenesis of oxidative phosphorylation complex I. *Cell Metab.* **12**, 283–294.
- Nowack, M.K., Harashima, H., Dissmeyer, N., Zhao, X.A., Bouyer, D., Weimer, A.K., De Winter, F. et al. (2012) Genetic framework of cyclin-dependent kinase function in Arabidopsis. *Dev. Cell*, **22**, 1030–1040.
- Owusu-Ansah, E., Yavari, A., Mandal, S. and Banerjee, U. (2008) Distinct mitochondrial retrograde signals control the G1-S cell cycle checkpoint. *Nat. Genet.* **40**, 356–361.
- Pedroli, D.B., Kuhm, C., Sevin, D.C., Vockenhuber, M.P., Sauer, U., Suess, B. and Mack, M. (2015) A dual control mechanism synchronizes riboflavin and sulphur metabolism in *Bacillus subtilis*. *Proc. Natl Acad. Sci. USA*, **112**, 14054–14059.
- Pinto, J.T. and Zemleni, J. (2016) Riboflavin. *Adv. Nutr.* **7**, 973–975.
- Powers, H.J. (2003) Riboflavin (vitamin B-2) and health. *Am. J. Clin. Nutr.* **77**, 1352–1360.
- Rendon, O.Z., Antonicka, H., Horvath, R. and Shoubridge, E.A. (2016) A mutation in the flavin adenine dinucleotide-dependent oxidoreductase FOXRED1 results in cell-type-specific assembly defects in oxidative phosphorylation complexes I and II. *Mol. Cell Biol.* **36**, 2132–2140.
- Sa, N., Rawat, R., Thornburg, C., Walker, K.D. and Roje, S. (2016) Identification and characterization of the missing phosphatase on the riboflavin biosynthesis pathway in *Arabidopsis thaliana*. *Plant J.* **88**, 705–716.
- Sabar, M., Balk, J. and Leaver, C.J. (2005) Histochemical staining and quantification of plant mitochondrial respiratory chain complexes using blue-native polyacrylamide gel electrophoresis. *Plant J.* **44**, 893–901.
- Sabelli, P.A. and Larkins, B.A. (2009) The development of endosperm in grasses. *Plant Physiol.* **149**, 14–26.
- Sabelli, P.A., Liu, Y., Dante, R.A., Lizarraga, L.E., Nguyen, H.N., Brown, S.W., Klingler, J.P. et al. (2013) Control of cell proliferation, endoreduplication, cell size, and cell death by the retinoblastoma-related pathway in maize endosperm. *Proc. Natl Acad. Sci. USA*, **110**, E1827–E1836.
- Salazar-Roa, M. and Malumbres, M. (2017) Fueling the cell division cycle. *Trends Cell Biol.* **27**, 69–81.
- Schmidt, R.J., Burr, F.A., Aukerman, M.J. and Burr, B. (1990) Maize regulatory gene opaque-2 encodes a protein with a "leucine-zipper" motif that binds to zein DNA. *Proc. Natl Acad. Sci.* **87**, 46–50.
- Sharma, P., Maklashina, E., Cecchini, G. and Iverson, T.M. (2019) Maturation of the respiratory complex II flavoprotein. *Curr. Opin. Struct. Biol.* **59**, 38–46.
- Sheridan, W. and Neuffer, G. (1983) Genetic control of embryo and endosperm development in maize. In *Gene Structure and Function in Higher Plants* (Reddy, G. and Coe, E., eds), pp. 105–122. New Delhi: Oxford and IBH Pub.
- Tyagi, S., Chabes, A.L., Wysocka, J. and Herr, W. (2007) E2F activation of S phase promoters via association with HCF-1 and the MLL family of histone H3K4 methyltransferases. *Mol. Cell*, **27**, 107–119.
- Venkatachalam, P., de Toledo, S.M., Pandey, B.N., Tephly, L.A., Carter, A.B., Little, J.B., Spitz, D.R. et al. (2008) Regulation of normal cell cycle progression by flavin-containing oxidases. *Oncogene*, **27**, 20–31.
- Wang, G., Fan, W., Ou, M., Wang, X., Qin, H., Feng, F., Du, Y. et al. (2019) Dek40 encodes a PBAC4 protein required for 20S proteasome biogenesis and seed development. *Plant Physiol.* **180**, 2120–2132.
- Wang, G., Sun, X.L., Wang, G.F., Wang, F., Gao, Q., Sun, X., Tang, Y.P. et al. (2011) Opaque7 encodes an acyl-activating enzyme-like protein that affects storage protein synthesis in maize endosperm. *Genetics*, **189**, 1281–1295.
- Wang, G., Wang, F., Wang, G., Wang, F., Zhang, X., Zhong, M., Zhang, J. et al. (2012) Opaque1 encodes a myosin XI motor protein that is required for endoplasmic reticulum motility and protein body formation in maize endosperm. *Plant Cell*, **24**, 3447–3462.
- Wang, G., Wang, H., Zhu, J., Zhang, X., Wang, F., Tang, Y. et al. (2010) An expression analysis of 57 transcription factors derived from ESTs of developing seeds in Maize (*Zea mays*). *Plant Cell Rep.* **29**, 545–559.
- Wang, G., Zhang, J.S., Wang, G.F., Fan, X.Y., Sun, X., Qin, H.L., Xu, N. et al. (2014) Proline responding1 plays a critical role in regulating general protein synthesis and the cell cycle in maize. *Plant Cell*, **26**, 2582–2600.
- Wang, G., Zhong, M.Y., Shuai, B.L., Song, J.D., Zhang, J., Han, L., Ling, H.L. et al. (2017) E plus subgroup PPR protein defective kernel 36 is required for multiple mitochondrial transcripts editing and seed development in maize and Arabidopsis. *New Phytol.* **214**, 1563–1578.
- Yang, J., Fu, M., Ji, C., Huang, Y. and Wu, Y. (2018) Maize Oxalyl-CoA decarboxylase1 degrades oxalate and affects the seed metabolome and nutritional quality. *Plant Cell*, **30**, 2447–2462.
- Yao, D.S., Qi, W.W., Li, X., Yang, Q., Yan, S.M., Ling, H.L., Wang, G. et al. (2016) Maize opaque10 encodes a cereal-specific protein that is essential for the proper distribution of zeins in endosperm protein bodies. *PLoS Genet.* **12**, e1006270.
- Zhang, J., Bonasio, R., Strino, F., Kluger, Y., Holloway, J.K., Modzelewski, A.J., Cohen, P.E. et al. (2013) SFMBT1 functions with LSD1 to regulate expression of canonical histone genes and chromatin-related factors. *Genes Dev.* **27**, 749–766.
- Zhang, S., Zhan, J. and Yadegari, R. (2018) Maize opaque mutants are no longer so opaque. *Plant Reprod.* **31**, 319–326.
- Zhang, Z.Y., Yang, J. and Wu, Y.R. (2015) Transcriptional regulation of zein gene expression in maize through the additive and synergistic action of opaque2, prolamine-box binding factor, and O2 heterodimerizing proteins. *Plant Cell*, **27**, 1162–1172.

Supporting information

Additional supporting information may be found online in the Supporting Information section at the end of the article.

Figure S1 SDS-PAGE analysis of total protein (A), zein (B) and nonzein (C) from mature endosperm of the wild type (WT) and *o18-1*. The size of each zein is indicated as the marker shown. M, protein markers in (A–C) from top to bottom correspond to 180, 130, 100, 70, 55, 40, 35, 25, 15 and 10 kD.

Figure S2 Developing ears (A) and seeds (B) showing the wild-type (WT) and *o18-1* phenotypes during kernel development. Bar is 1 cm. DAP, days after pollination.

Figure S3 Expression levels of BETL-related genes in WT and *o18-1* kernels at 15 and 20 DAP. For each RNA sample, three technical replicates were performed. Representative results from three biological replicates are shown. Error bars represent SE. Transcript abundance is indicated relative to the internal control *Ubiquitin (UBQ)*.

Figure S4 DNA sequence mutation determination of the three *o18* alleles. (A) A G-to-A transition occurs at exon 4 of *Zm00001d16902* in *o18-1* causing a residue substitution from G-to-E. (B) Association analysis of the mutation site of *o18-1* in the representative maize inbred lines using a specific dCAPS marker. (C) A C-to-T transition occurs at exon 2 of *Zm00001d16902* in *o18-2* causing a residue substitution from Q-to-stop. (D) DNA sequence identification of the CRISPR/Cas9-edited allele *o18-3*. A single-guide RNA (sgRNA) is designed crossing the boundary between exon 2 and intron 2, which leads to a 5-bp deletion (marked in red) and a splicing error. The box marks partial of exon 2.

Figure S5 Phylogenetic topology of RIBA orthologues from Gramene. Ensembl gene trees are generated by the Gene Orthology/Paralogy prediction method pipeline. The display shows the maximum likelihood phylogenetic tree representing the evolutionary history of genes. These trees are reconciled with a species tree, generated by TreeBeST. Internal nodes are then annotated for duplication (red boxes) or speciation (blue boxes) events. The maize RIBA paralogues are highlighted in colour.

Figure S6 Comparison of the coding domains and expression patterns of maize *RIBA* genes. (A) and (B) Sequence alignments of DHBPS (A) and GCH II (B) in the O18 protein and its homologues from *Arabidopsis* and maize. The residues essential for enzyme activities are indicated in coloured shapes. Blue box, the conserved amino acid sequences; orange box, the enzymatically important amino acid residues; Red box, residue substitution or deletion in the catalytic or substrate-binding domains. Black box, residual changes in the zinc-binding region of *ZmRIBA3*. (C) Heat maps showing development- and anatomy-specific expression profiles of the maize *RIBA* genes. Public expression data sets were retrieved from MaizeGDB. The colour bar represents the expression values. Data shown are \log_2 (FPKM). FPKM, fragments per kilobase per million.

Figure S7 *ZmRIBA2* is a pseudogene. (A) RNA expression levels of *ZmRIBA2* in various tissues. cDNA from *O18* (+/+) and *o18-1* (–/–) was used as controls. (B) Spatial and temporal expression patterns of *P_{ZmRIBA2}:GUS* transgenic *Arabidopsis* plants.

Figure S8 Punctuate structures of O18-GFP in chloroplasts. The fusion protein O18-GFP was transiently expressed in tobacco leaf mesophyll cells, infiltrated with different concentrations. Bar is 20 μ m.

Figure S9 Functional complementation of *E. coli* knock-out strain BSV18 (*ribA18::Tn5*; CGSC# 6992) *ArbA* mutant by using the GCH II domains of *O18* and *ZmRIBA3*. Transformants were incubated on LB medium containing chloramphenicol, without riboflavin (LB/+Chl/-riboflavin) or plus riboflavin (LB/+Chl/+riboflavin).

Figure S10 Transcriptomic analysis of differentially expressed genes (DEGs) in endosperm at 18 DAP between *o18-1* and the wild type. (A) Gene ontology (GO) enrichment analysis of the 886 functional annotated DEGs. The number of genes and P value of each term are listed in detail. (B) Expression levels of histone genes in WT and *o18-1* kernels at 10 and 15 DAP. For each RNA sample, three technical replicates were performed. Representative results from three biological replicates are shown. Error bars represent SE. Transcript abundance is indicated relative to the internal control *Ubiquitin (UBQ)*.

Figure S11 Heat maps showing RBR1 targets differentially expressed in endosperm transcriptome at 18 DAP between *o18-1* and the wild type. The colour bar represents the expression values of *o18/WT*.

Figure S12 Identification and analysis of *LSD1*-like genes in maize. (A) Phylogenetic tree of maize *LSD1*-like proteins. Maize and *Arabidopsis* *LSD1* homologues were aligned by ClustalW. The phylogenetic tree was constructed using MEGA 7.0. At, *Arabidopsis thaliana*; Zm, *Zea mays*. (B) Expression levels of *LSD1*-like genes in WT and *o18-1* kernels at 10 and 15 DAP. For each RNA sample, three technical replicates were performed. Representative results from three biological replicates are shown. Error bars represent SE. Transcript abundance is indicated relative to the internal control *Ubiquitin (UBQ)*.

Figure S13 Model depicting the function of riboflavin in integrating cellular energy and cell cycle to modulate maize endosperm development. In the wild type, riboflavin is *de novo* synthesized in plastid, and the subsequent FMN and FAD are synthesized in either plastid, cytoplasm or mitochondrion. FMN and FAD primarily act as electron carriers, coupling to proton generation in mitochondrial complex I and complex II. FAD also decorates several proteins that are required for assembly, maturation and stability of the complexes. The energy thus fuels the G1/S transition in both mitotic and endoreduplicating endosperm cell cycles, in a cyclin D-CDKA-RBR-E2F-dependent fashion. In *o18* mutant, lack of riboflavin, FMN and FAD impairs cellular energetics by disrupting mitochondrial complex I and complex II assembly and activity. Deprivation of energy leads to G1 and S phases arrest of endosperm cells, by undermining CDKA activity or triggering specific cell-cycle checkpoints. The inducing of cell-cycle genes in *o18* is associated with the increase of their H3K4me3 marks, which is probably caused by dysfunction of *LSD1*-like proteins. Therefore, we assume that H3K4 methylation-mediated epigenetic regulation could be a back-up mechanism of cell-cycle progression in nutrient-deficient and energy-insufficient adaptation.

Table S1 Chi-square tests of the mature kernel phenotypes in *o18-1* F₂ ears.

Table S2 List of primers used in this study.

Table S3 A summary of candidate genes of maize mutant *O18*.

Table S4 Allelism tests using heterozygous *o18-1* and homozygous *o18-2* and *o18-3* T3 plants.

Table S5 Chi-square tests of seed phenotypes in *atribal* F₂ population.

Table S6 List of constructs used in this study.